J. Fluid Mech. (2008), *vol.* 600, *pp.* 339–371. © 2008 Cambridge University Press
doi:10.1017/S0022112008000505 Printed in the United Kingdom

Lateral dispersion in random cylinder arrays at high Reynolds number

YUKIE TANINO AND HEIDI M. NEPF
Department of Civil and Environmental Engineering, Massachusetts Institute of Technology,
Cambridge, MA 02139, USA
ytanino@alum.mit.edu; hmnepf@mit.edu

(Received 27 March 2007 and in revised form 26 December 2007)

Laser-induced fluorescence was used to measure the lateral dispersion of passive solute in random arrays of rigid, emergent cylinders of solid volume fraction $\phi = 0.010$–0.35. Such densities correspond to those observed in aquatic plant canopies and complement those in packed beds of spheres, where $\phi \geqslant 0.5$. This paper focuses on pore Reynolds numbers greater than $Re_s = 250$, for which our laboratory experiments demonstrate that the spatially averaged turbulence intensity and $K_{yy}/(U_p d)$, the lateral dispersion coefficient normalized by the mean velocity in the fluid volume, U_p, and the cylinder diameter, d, are independent of Re_s. First, $K_{yy}/(U_p d)$ increases rapidly with ϕ from $\phi = 0$ to $\phi = 0.031$. Then, $K_{yy}/(U_p d)$ decreases from $\phi = 0.031$ to $\phi = 0.20$. Finally, $K_{yy}/(U_p d)$ increases again, more gradually, from $\phi = 0.20$ to $\phi = 0.35$. These observations are accurately described by the linear superposition of the proposed model of turbulent diffusion and existing models of dispersion due to the spatially heterogeneous velocity field that arises from the presence of the cylinders. The contribution from turbulent diffusion scales with the mean turbulence intensity, the characteristic length scale of turbulent mixing and the effective porosity. From a balance between the production of turbulent kinetic energy by the cylinder wakes and its viscous dissipation, the mean turbulence intensity for a given cylinder diameter and cylinder density is predicted to be a function of the form drag coefficient and the integral length scale l_t. We propose and experimentally verify that $l_t = \min\{d, \langle s_n \rangle_A\}$, where $\langle s_n \rangle_A$ is the average surface-to-surface distance between a cylinder in the array and its nearest neighbour. We farther propose that only turbulent eddies with mixing length scale greater than d contribute significantly to net lateral dispersion, and that neighbouring cylinder centres must be farther than r^* from each other for the pore space between them to contain such eddies. If the integral length scale and the length scale for mixing are equal, then $r^* = 2d$. Our laboratory data agree well with predictions based on this definition of r^*.

1. Introduction

Turbulence and dispersion in obstructed flows have been investigated for decades because of their relevance to transport in groundwater (e.g. Bear 1979), to transport in flow around buildings (e.g. Davidson *et al.* 1995) and trees (e.g. Kaimal & Finnigan 1994, chapter 3), and to engineering applications such as contaminant transport and removal in artificial wetlands (Serra, Fernando & Rodriguez 2004). In particular, flow in a packed bed of spheres has been examined intensively, and analytical descriptions of different mechanisms that contribute to dispersion in Stokes flow were derived

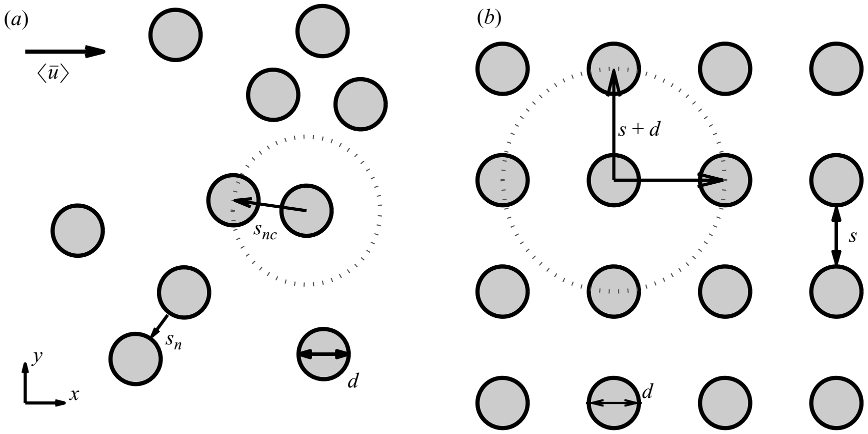

FIGURE 1. Definition of key geometric parameters for an array of cylinders of uniform diameter d. (a) In a random array, the centre-to-centre distance to the nearest neighbour, s_{nc}, differs for each cylinder. (b) In a periodic square array, the centre-to-centre distance to the nearest neighbour is $s + d \equiv 1/\sqrt{m}$ for all cylinders, where m is the number of cylinders per unit area.

by Koch & Brady (1985). In packed beds of spheres, the solid volume fraction ϕ is approximately constant at $\phi \approx 0.6$ (e.g. Mickley, Smith & Korchak 1965; Jolls & Hanratty 1966; Han, Bhakta & Carbonell 1985; Yevseyev, Nakoryakov & Romanov 1991; Dullien 1979, p. 132). In contrast, previous studies on emergent (i.e. spanning the water column and penetrating the free surface), rigid aquatic vegetation have focused on low solid volume fraction arrays ($\phi = 0.0046$–0.063, e.g. Nepf, Sullivan & Zavistoski 1997; White & Nepf 2003). Such sparse arrays are characteristic of salt marshes, for example, where $\phi = 0.001$–0.02 (Valiela, Teal & Deuser 1978; Leonard & Luther 1995). However, ϕ in aquatic plant canopies can approach that of packed beds. In mangroves, for example, ϕ can reach 0.45 because of the dense network of roots (Mazda *et al.* 1997). In constructed wetlands, ϕ may extend to 0.65 (Serra *et al.* 2004), and in this context Serra *et al.* (2004) reported lateral dispersion measurements at low Reynolds numbers in random arrays of $\phi = 0.10, 0.20$ and 0.35. This paper investigates turbulence and solute transport in arrays of randomly distributed, emergent, rigid cylinders of $\phi = 0.010$–0.35 in turbulent flow. Models for turbulence intensity and net lateral dispersion are presented and verified with laboratory measurements.

In § 2, we present a model for the mean turbulence intensity and the lateral dispersion coefficient as a function of cylinder distribution and cylinder density. In § 3, the experimental procedure for measuring turbulence, the integral length scale and net lateral dispersion is described. In § 4, the experimental results are presented and compared with the theory. Also, in Appendix A, analytical expressions of nearest-neighbour distances in a random array of cylinders of finite volume are presented, and parameters relevant to the models are derived.

2. Background theory

We consider a homogeneous, two-dimensional array of rigid circular cylinders of uniform diameter d distributed randomly with a constant density m (cylinders per unit horizontal area). The corresponding solid volume fraction is $\phi = m\pi d^2/4$. The centre-to-centre distance from a particular cylinder to its nearest neighbour is denoted by s_{nc}, as illustrated in figure 1(a) for an arbitrary cylinder. The corresponding surface-to-surface distance is denoted by s_n $(=s_{nc}-d)$. Analytical expressions of $\langle s_n\rangle_A$, the mean nearest-neighbour separation defined between cylinder surfaces, are derived in Appendix A. $\langle\ \rangle_A$ denotes an average over many cylinders in the array. The Cartesian coordinates $\boldsymbol{x}=(x,y,z)=(x_1,x_2,x_3)$ are defined such that the x-axis is aligned with $\langle\bar{u}\rangle$, the fluid velocity averaged over time and the fluid volume. The y-axis is in the horizontal plane and perpendicular to the x-axis (figure 1*a*). The vertical z-axis is aligned with the cylinder axes. Flow in a cylinder array is characterized by the cylinder Reynolds number, $Re_d\equiv\langle\bar{u}\rangle d/\nu$, where ν is the kinematic viscosity, as well as the Reynolds number based on a mean pore scale, $Re_s\equiv\langle\bar{u}\rangle s/\nu$. Here, the mean pore scale $s\equiv 1/\sqrt{m}-d$ is defined as the surface-to-surface distance between aligned cylinders in a square array with the same ϕ, as illustrated in figure 1(*b*).

2.1. *Solute transport in a random array*

Species conservation is described by the expression

$$\frac{\partial c}{\partial t}+\boldsymbol{v}\cdot\nabla c=-\nabla\cdot(-D_0\nabla c),\tag{2.1}$$

where t is time, $c(\boldsymbol{x},t)$ is the solute concentration, $\boldsymbol{v}(\boldsymbol{x},t)=(u,v,w)=(v_1,v_2,v_3)$ is the fluid velocity and D_0 is the molecular diffusion coefficient. In obstructed turbulent flows, it is convenient to first decompose c and $\boldsymbol{v}$ into a local time average and instantaneous deviations from that average, and to farther decompose the time-averaged parameters into a spatial average and local deviations from that average (e.g. Raupach & Shaw 1982; Finnigan 1985). The temporal averaging operation, denoted by an overbar, is defined with a time interval much longer than the time scales of turbulent fluctuations and vortex shedding. The spatial averaging operation, denoted by $\langle\ \rangle$, is defined with an infinitesimally thin volume interval V_f that spans many cylinders. The solid (cylinder) volume is excluded from V_f. Then, $c=\langle\bar{c}\rangle(\boldsymbol{x},t)+\bar{c}''(\boldsymbol{x},t)+c'(\boldsymbol{x},t)$ and $\boldsymbol{v}=\langle\bar{\boldsymbol{v}}\rangle(\boldsymbol{x},t)+\bar{\boldsymbol{v}}''(\boldsymbol{x},t)+\boldsymbol{v}'(\boldsymbol{x},t)$, where $^{-\prime\prime}$ denotes the spatial fluctuations of the temporal average and $'$ denotes the temporal fluctuations. By definition, $\overline{c'}$, $\overline{\boldsymbol{v}'}$, $\langle\bar{c}''\rangle$, $\langle\bar{\boldsymbol{v}}''\rangle=0$. Also, $\langle\bar{v}\rangle=\langle\bar{w}\rangle=0$. Substituting these expressions into (2.1), averaging over the same temporal and spatial intervals, and retaining only the dominant terms yield (Finnigan 1985, equation 21)

$$\frac{\partial\langle\bar{c}\rangle}{\partial t}+\langle\bar{v}_j\rangle\frac{\partial\langle\bar{c}\rangle}{\partial x_j}=-\frac{\partial}{\partial x_j}\left\{\left\langle\overline{v_j'c'}\right\rangle+\langle\bar{v}_j''\bar{c}''\rangle-D_0\left\langle\frac{\partial}{\partial x_j}(\langle\bar{c}\rangle+\bar{c}'')\right\rangle\right\}.\tag{2.2}$$

In addition to fluxes associated with the local temporal fluctuations, $\left\langle\overline{\boldsymbol{v}'c'}\right\rangle$, the averaging scheme introduces dispersive fluxes associated with the time-averaged spatial fluctuations, $\langle\bar{\boldsymbol{v}}''\bar{c}''\rangle$.

Laboratory measurements by White & Nepf (2003) and in the present study (see figure 16) suggest that *net* dispersion is Fickian. Then, (2.2) simplifies to

$$\frac{\partial\langle\bar{c}\rangle}{\partial t}+\langle\bar{v}_j\rangle\frac{\partial\langle\bar{c}\rangle}{\partial x_j}=K_{jj}\frac{\partial^2\langle\bar{c}\rangle}{\partial x_j^2},\tag{2.3}$$

where K_{jj} are the coefficients for net dispersion. In this paper, we are concerned with K_{yy}, the net lateral dispersion coefficient.

Farthermore, $\langle\overline{\boldsymbol{v}'c'}\rangle$ and $\langle\bar{\boldsymbol{v}}''\bar{c}''\rangle$, like molecular diffusion, are expected to be Fickian if the spatial scale of the contributing mechanisms is smaller than the scale over which the mean concentration gradient varies (Corrsin 1974; Koch & Brady 1985; White & Nepf 2003). The two mechanisms associated with $\left\langle\overline{v'c'}\right\rangle$ and $\langle\bar{v}''\bar{c}''\rangle$, as identified below, both have characteristic scales of d and $\langle s_n\rangle_A$ (§ 2.2 and § 2.3).

Because the dimensions of the averaging volume V_f are much larger than d and $\langle s_n \rangle_A$ by definition, $\langle \bar{c} \rangle$ is expected to vary slowly at these spatial scales. Therefore, $\langle \overline{v'c'} \rangle$ and $\langle \overline{v}''\overline{c}'' \rangle$ are expected to be Fickian. Consequently, K_{yy} is expected to be the linear sum of three constant coefficients, one that parameterizes $\langle \overline{v'c'} \rangle$, one that parameterizes $\langle \overline{v}''\overline{c}'' \rangle$ and the molecular diffusion coefficient. The first two coefficients represent, respectively, (i) turbulent diffusion and (ii) mechanical dispersion (i.e. independent of molecular diffusion) due to the spatially heterogeneous velocity field generated by the randomly distributed cylinders. In this paper, the two processes are treated as independent, and one is not considered in the description of the other. Molecular diffusion is negligible, as we only consider turbulent flow.

2.2. *Contribution from turbulence*

The classic scaling for turbulent diffusion is $K_{yy} \sim \langle \sqrt{k_t} \rangle l_e$, where l_e is the length scale associated with mixing due to turbulent eddies and $k_t \equiv (\overline{u'^2} + \overline{v'^2} + \overline{w'^2})/2$ is the turbulent kinetic energy per unit mass (e.g. Baldyga & Bourne 1999, chapter 4). Previously, Nepf (1999) assumed that, in a cylinder array, l_e is equal to the integral length scale of the largest turbulent eddies, l_t, and that $l_t = d$ when cylinder spacing is smaller than the water depth. Then, $K_{yy} \sim \langle \sqrt{k_t} \rangle d$. Nepf (1999) fitted this turbulent diffusion scale to experimental observation at $Re_s = U_p s/\nu = 2000\text{–}10\,000$ in a $\phi = 0.0046$, periodic, staggered cylinder array (see Zavistoski 1994 for the exact cylinder configuration) to obtain

$$\frac{K_{yy}}{U_p d} = 0.9 \left\langle \frac{\sqrt{k_t}}{U_p} \right\rangle . \tag{2.4}$$

The mean pore velocity U_p is the average of $\overline{u}$ over all fluid volume within the array, and is determined as $U_p = Q/[\langle \overline{H} \rangle W(1-\phi)]$, where Q is the volumetric flow rate, $\langle \overline{H} \rangle$ is the mean water depth and W is the width of the laboratory flume in which the array was contained. Note that $\langle \overline{u} \rangle \approx U_p$ if the thickness of the boundary layers at the bed and sidewalls of the flume is negligible relative to $\langle \overline{H} \rangle$ and W. Equation (2.4) is inconsistent with experiment at high ϕ, as will be demonstrated in § 4.3. Below, we propose a new scale model for turbulent diffusion, in which l_e and l_t may be constrained by cylinder spacing at high ϕ.

2.2.1. *Turbulence intensity*

The functionality of the mean turbulence intensity, $\langle \sqrt{k_t}/\langle \overline{u} \rangle \rangle$, can be predicted from the temporally and spatially averaged mean and turbulent kinetic energy budgets in the array (see e.g. Raupach, Antonia & Rajagopalan 1991, equation 4.3*a*, *b* or Kaimal & Finnigan 1994, equation 3.40 for the turbulent kinetic energy budget). In cylinder arrays, a wake production term, $-\left\langle \overline{u_i'u_j'}'' \partial \overline{u_i}''/\partial x_j \right\rangle$ ($\geqslant 0$), accounts for turbulence production by the cylinder wakes. Numerical simulation by Burke & Stolzenbach (1983, figure 5.23) demonstrates for $C_D \langle \overline{H} \rangle \phi/(\pi d/4) = 0.01\text{–}1.0$, where C_D is the coefficient of mean cylinder drag, that wake production exceeds production due to shear within the cylinder array, except near the bed. In fully developed flow with negligible shear production, the turbulent kinetic energy budget reduces to a balance between wake production and viscous dissipation of turbulent kinetic energy (e.g. Burke & Stolzenbach 1983; Raupach & Shaw 1982):

$$0 \approx -\left\langle \overline{u_i'u_j'}'' \frac{\partial \overline{u_i}''}{\partial x_j} \right\rangle - \nu \left\langle \overline{\frac{\partial u_i{}'}{\partial x_j} \frac{\partial u_i{}'}{\partial x_j}} \right\rangle . \tag{2.5}$$

Similarly, the mean kinetic energy budget reduces to

$$0 \approx \langle \overline{u_i} \rangle f_i^{form} + \left\langle \overline{u_i' u_j'}'' \frac{\partial \overline{u_i}''}{\partial x_j} \right\rangle + \nu \langle \overline{u_i}'' \nabla^2 \overline{u_i}'' \rangle, \tag{2.6}$$

where

$$f_i^{form} = \frac{1}{\rho V_f} \iint_{S_c} \overline{p} n_i \, \mathrm{d}S \quad (\geqslant 0) \tag{2.7}$$

is the hydrodynamic force per unit fluid mass exerted on S_c that arises from the pressure loss in cylinder wakes, where S_c denotes all cylinder surfaces that intersect V_f, $\boldsymbol{n}$ is the unit normal vector on S_c pointing out of V_f, $p(\boldsymbol{x}, t)$ is the local pressure and ρ is the fluid density.

The Kolmogorov microscale η estimated from our laser Doppler velocimetry (LDV) measurements (see § 3) ranged from $\eta/d = 0.0014$ to $\eta/d = 0.21$ and $\eta/\langle s_n \rangle_A = 0.0036$ to $\eta \langle s_n \rangle_A = 0.83$. These $O(0.001\text{–}1)$ ratios suggest that wake production is a more significant sink of mean kinetic energy than the viscous term $\nu \langle \overline{u_i}'' \nabla^2 \overline{u_i}'' \rangle$ (Raupach & Shaw 1982). For simplicity, the latter is neglected in (2.6), which yields a balance between the rate of work done by form drag and wake production (Raupach & Shaw 1982, equation 17):

$$0 \approx \langle \overline{u_i} \rangle f_i^{form} + \left\langle \overline{u_i' u_j'}'' \frac{\partial \overline{u_i}''}{\partial x_j} \right\rangle . \tag{2.8}$$

Note that $i = 1$ is the only non-zero component of $\langle \overline{u_i} \rangle f_i^{form}$. Combining (2.5) and (2.8) and replacing the viscous dissipation term with the classic scaling, $\sqrt{k_t}^3 / l_t$ (Tennekes & Lumley 1972), yield a model for mean turbulence intensity:

$$\left\langle \frac{\sqrt{k_t}}{\langle \overline{u} \rangle} \right\rangle \sim \left[\frac{\langle \overline{f_D} \rangle^{form}}{\rho \langle \overline{u} \rangle^2 d/2} \frac{l_t}{d} \frac{m d^2}{2(1-\phi)} \right]^{1/3}, \tag{2.9}$$

where $\langle \overline{f_D} \rangle^{form} \equiv \rho(1-\phi) f_1^{form}/m$ is the inertial contribution to the mean drag (in the direction of mean flow) per unit length of cylinder. Tanino & Nepf (2008, $d = 0.64$ cm) determined the following empirical relation for $\langle \overline{f_D} \rangle_H^{form}$, the depth average of $\langle \overline{f_D} \rangle^{form}$:

$$\frac{\langle \overline{f_D} \rangle_H^{form}}{\rho U_p^2 d/2} = 2 \left[(0.46 \pm 0.11) + (3.8 \pm 0.5)\phi \right]. \tag{2.10}$$

For convenience, we define a drag coefficient that represents this contribution:

$$C_D^{form} \equiv \frac{\langle \overline{f_D} \rangle_H^{form}}{\rho U_p^2 d/2}. \tag{2.11}$$

Laboratory measurements suggest that temporally and spatially averaged flow properties in Tanino & Nepf (2008)'s laboratory experiments and in the present study were approximately uniform vertically (e.g. figure 8; White & Nepf 2003) and laterally (e.g. figure 7; White & Nepf 2003). Consequently, $\langle \overline{f_D} \rangle^{form} \approx \langle \overline{f_D} \rangle_H^{form}$ and $\langle \overline{u} \rangle \approx U_p$. Then, (2.9) can be rewritten as:

$$\left\langle \frac{\sqrt{k_t}}{\langle \overline{u} \rangle} \right\rangle \approx \left\langle \frac{\sqrt{k_t}}{U_p} \right\rangle \sim \left[C_D^{form} \frac{l_t}{d} \frac{\phi}{(1-\phi)\pi/2} \right]^{1/3}, \tag{2.12}$$

where C_D^{form} is described by (2.10) and (2.11). Recall that $m = \phi/(\pi d^2/4)$.

The choice of $l_t = d$ is the convention in the literature on flow through vegetation (e.g. Raupach & Shaw 1982; Raupach *et al.* 1991) and is reasonable in sparse arrays

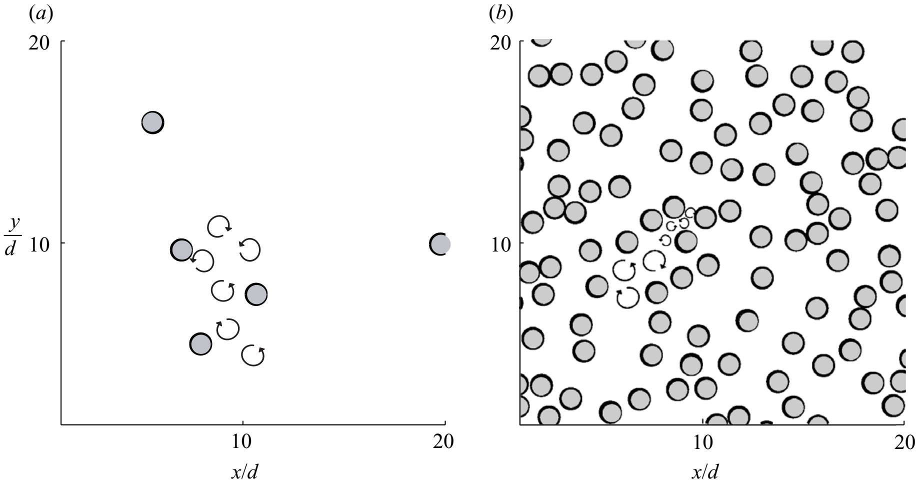

FIGURE 2. A section of simulated arrays of (a) $\phi = 0.010$, $d < \langle s_n \rangle_A$ and (b) $\phi = 0.20$, $d > \langle s_n \rangle_A$. Circles represent cylinders, to scale. Turbulent eddies, depicted by the arrows, are $O(d)$ in sparse arrays, but are constrained by the local cylinder separation where the pore length scale is smaller than d.

(figure 2a). In dense arrays, however, the local pore length scale may be less than $O(d)$. In these regions, physical reasoning suggests that the local cylinder spacing will constrain the eddies (figure 2b). Therefore, l_t must be redefined at high ϕ. The simplest function consistent with the expected dependence on the local surface-to-surface distance between cylinders is

$$l_t = \min\{d,\ \langle s_n \rangle_A\}. \tag{2.13}$$

2.2.2. *Turbulent diffusion coefficient*

We expect the spatially heterogeneous velocity field to induce lateral deflections of $O(d)$ per cylinder in the dispersion mechanism described in § 2.3 (e.g. Masuoka & Takatsu 1996; Nepf 1999). Therefore, we propose that only turbulent eddies with mixing length scale $l_e \geqslant d$ contribute significantly to net lateral dispersion relative to the spatially heterogeneous velocity field. Let r^* be the minimum distance between cylinder centres that permits the pore space constrained by them to contain such eddies. Physical reasoning suggests that the mixing length scale associated with turbulent eddies is approximately equal to the size of the eddies, i.e. $l_e \approx l_t$, which, together with (2.13), implies $r^* - d = d$. Then, within an infinitesimally thin section of the array whose total (solid and fluid) volume is denoted by V, the sum of all volume that contributes to turbulent diffusion, V_m ($\leqslant V$), is a sum of all pore space with length greater than $r^* - d$. Within these pores, $l_e = d$. To simplify, we associate all fluid volume with a cylinder. Farther, each cylinder in the array has a fluid volume around it of characteristic horizontal area s_n^2. Then,

$$V_m = \left\langle s_n^2 \right\rangle_{s_{nc} > r^*} N_{s_{nc} > r^*}, \tag{2.14}$$

where $N_{s_{nc} > r^*}$ is the number of cylinders with $s_{nc} > r^*$ in V. Recall that $s_{nc} = s_n + d$.

To define K_{yy} as an average over both fluid and solid volume, local $\sqrt{k_t} l_e$ is integrated over V_m and divided by V. Then, the contribution from turbulent diffusion is

$$\frac{K_{yy}}{\langle \overline{u} \rangle d} = \gamma_1 \frac{\langle \sqrt{k_t} l_e \rangle_m}{\langle \overline{u} \rangle d} \frac{V_m}{V}, \tag{2.15}$$

where $\langle\ \rangle_m$ denotes a spatial average over V_m and γ_1 is the scaling constant. Equation (2.15) is simplified by neglecting the cross-correlations such that $\langle \sqrt{k_t} l_e \rangle_m = \langle \sqrt{k_t} \rangle_m \langle l_e \rangle_m$ and assuming that $\langle \sqrt{k_t} \rangle_m = \langle \sqrt{k_t} \rangle$, the average over all fluid volume. Equation (2.15) then becomes

$$\frac{K_{yy}}{\langle \overline{u} \rangle d} \approx \gamma_1 \left\langle \frac{\sqrt{k_t}}{\langle \overline{u} \rangle} \right\rangle \frac{\langle s_n^2 \rangle_{s_{nc} > r^*}}{d^2} \frac{\phi}{\pi/4} P_{s_{nc} > r^*}, \tag{2.16}$$

where $P_{s_{nc} > r^*} \equiv N_{s_{nc} > r^*}/(mV)$ is the fraction of cylinders with a nearest neighbour farther than r^* (centre-to-centre) from its centre. Recall that $\langle \sqrt{k_t} / \langle \overline{u} \rangle \rangle$ can be described by (2.12) and (2.13), given d and ϕ.

2.3. *Contribution from the time-averaged, spatially heterogeneous velocity field*

Two existing models of lateral dispersion due to the spatially heterogeneous velocity field are considered in this paper. The simplest model describes the lateral deflection of fluid particles due to the presence of the cylinders as a one-dimensional random walk (Nepf 1999). In this model, a fluid particle is considered to undergo a sequence of independent and discrete lateral displacements of equal length, where each displacement has equal probability of being in the positive or in the negative y direction. The long-time lateral dispersion of many such fluid particles is described by:

$$\frac{K_{yy}}{\langle \overline{u} \rangle d} = \frac{1}{2} \left(\frac{\epsilon}{d} \right)^2 \frac{\phi}{\pi/4}, \tag{2.17}$$

where ϵ, the magnitude of each displacement, is a property of the cylinder configuration and Re_d. Nepf (1999) proposed that $\epsilon = d$. With this assumption, (2.17) becomes a function of ϕ only.

The second model considered for this mechanism is Koch & Brady (1986)'s analytical solution for mechanical dispersion due to two-cylinder interactions in Stokes flow, with a modification to only include cylinders with a nearest neighbour sufficiently close to permit cylinder–cylinder interaction. Analytical solutions for long-time Fickian dispersion in a homogeneous, sparse, random cylinder array were derived for Stokes flow by Koch & Brady (1986) by averaging the governing equations over an ensemble of arrays with different cylinder configurations. Neglecting molecular diffusion, lateral dispersion arises from the velocity disturbances induced by the randomly distributed cylinders (Koch & Brady 1986). The authors demonstrate that this hydrodynamic dispersion consists of a mechanical component and non-mechanical corrections, but that only the mechanical contribution, associated with the spatially heterogeneous velocity field due to the obstacles, has a non-zero lateral component. Farther, the authors showed that, because of their fore–aft symmetry, circular cylinders do not contribute to lateral dispersion unless two-cylinder interactions are considered. Taking into consideration such interactions, Koch & Brady (1986) determined that the mechanical contribution of the cylinder array in Stokes flow is

$$\frac{K_{yy}}{\langle \overline{u} \rangle d} = \frac{\pi}{4096} \left(\frac{d^2}{k_\perp} \right)^{3/2} \frac{1 - \phi}{\phi^2}, \tag{2.18}$$

where $k_\perp$ is the permeability such that the mean drag (in the direction of mean flow) per unit length of cylinder is

$$\langle \overline{f_D} \rangle = \frac{\pi}{4}\frac{d^2}{k_\perp}\mu\langle \overline{u}\rangle \frac{1-\phi}{\phi}, \tag{2.19}$$

where μ is the dynamic viscosity. Numerical simulations show that $d^2 k_\perp^{-1}$ increases monotonically with ϕ (Koch & Ladd 1997). For sparse random arrays, $k_\perp$ is accurately described by Spielman & Goren (1968)'s analytical solution (B 1). For dense arrays, Koch & Ladd (1997) have shown that a theoretical model based on the lubrication approximation accurately captures the dependence of $k_\perp$ on the characteristic distance between neighbouring cylinders. The permeability $k_\perp$ for arrays of intermediate density, for which analytical expressions have not been derived, can be described by an empirical fit to numerical simulation data (B 3). Models for $k_\perp$ relevant to our laboratory experiments are discussed in Appendix B.

Equation (2.18), where $k_\perp$ is described by (B 1), predicts that dispersion due to two-cylinder interactions will increase as ϕ decreases below $\phi = 0.017$. Koch & Brady (1986) attribute this predicted increase to the increase in the average distance over which velocity disturbances induced by a cylinder decay. This distance, known as the Brinkman screening length, scales with the square root of permeability. As discussed in Appendix B, $\sqrt{k_\perp} \approx \langle s_n\rangle_A$ in sparse arrays. However, the fraction of cylinders with a neighbour close enough to result in cylinder–cylinder interaction decreases with decreasing ϕ, and physical reasoning suggests that the contribution from this process approaches zero as ϕ decreases to zero. Therefore, we introduce an adjustment to Koch & Brady (1986)'s solution. Previous studies in unsteady and turbulent flow report interacting wakes between side-by-side cylinders with a centre-to-centre distance less than $5d$ (e.g. Zhang & Zhou 2001; Meneghini *et al.* 2001). Similarly, the drag on a cylinder is influenced by the presence of a neighbouring cylinder that is within $5d$ (Petryk 1969). Following these studies, we assume that only cylinders whose centres are within $5d$ of another cylinder centre contribute to net dispersion through this mechanism. Accordingly, Koch & Brady (1986)'s solution is multiplied by the fraction of cylinders that have a nearest neighbour within $5d$, $P_{s_{nc}<5d}$. We assume that this process is otherwise unaffected by inertia. In addition, a scaling constant γ_2 is introduced. After the introduction of these two terms, Koch & Brady (1986)'s solution becomes

$$\frac{K_{yy}}{\langle \overline{u}\rangle d} = \gamma_2 P_{s_{nc}<5d}\frac{\pi}{4096}\left(\frac{d^2}{k_\perp}\right)^{3/2}\frac{1-\phi}{\phi^2}. \tag{2.20}$$

2.4. *Coefficient for net lateral dispersion*

Finally, an expression for net lateral dispersion is given by the linear superposition of the models for turbulent diffusion and dispersion due to the spatially heterogeneous velocity field. For example, superposing (2.16) and the proposed modification of Koch & Brady (1986)'s solution (2.20) yields

$$\frac{K_{yy}}{\langle \overline{u}\rangle d} = \gamma_1 \frac{4}{\pi}\phi \left\langle \frac{\sqrt{k_t}}{\langle \overline{u}\rangle} \right\rangle P_{s_{nc}>r^*}\frac{\langle s_n^2\rangle_{s_{nc}>r^*}}{d^2} + \gamma_2 P_{s_{nc}<5d}\frac{\pi}{4096}\left(\frac{d^2}{k_\perp}\right)^{3/2}\frac{1-\phi}{\phi^2}. \tag{2.21}$$

To permit an analytical expression for (2.21), $P_{s_{nc}>r^*}$ and $P_{s_{nc}<5d}$ are approximated as the probability that a single cylinder in a random array will have a nearest neighbour farther away than $r = r^*$ and within $r = 5d$, respectively, where r is the radial coordinate defined with the origin at the centre of that cylinder. Analytical expressions

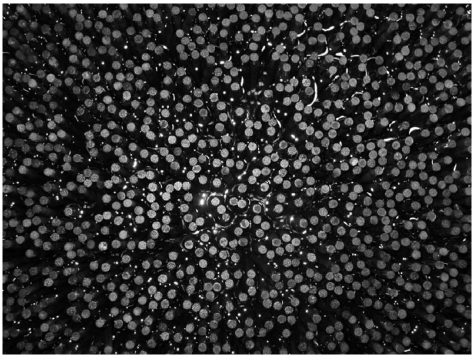

FIGURE 3. A photo of a section of the model $\phi = 0.27$ array in plan view.

for $P_{s_{nc} > r^*}$, $P_{s_{nc} < 5d}$ and $\langle s_n^2 \rangle_{s_{nc} > r^*}$ for the random arrays used in the present laboratory experiments are derived in Appendix A. Note that $P_{s_{nc} < 5d}$ approaches 1 monotonically as ϕ increases from zero, with $P_{s_{nc} < 5d} > 0.99$ at $\phi \geqslant 0.043$. Expressions for $k_\perp$ are presented in Appendix B.

3. Experimental procedure

Laboratory experiments were conducted to verify the definition of l_t (2.13) and the scale model for $\langle \sqrt{k_t}/\langle \overline{u} \rangle \rangle$ (2.12) and to document the ϕ dependence of $K_{yy}/(\langle \overline{u} \rangle d)$. Scaling constants in (2.12) and the model for $K_{yy}/(\langle \overline{u} \rangle d)$ (2.21) were determined from the experimental data.

The laboratory study consisted of two parts: measuring velocity and imaging the lateral concentration profile of a passive tracer. In both parts, cylindrical maple dowels of diameter $d = 0.64$ cm (Saunders Brothers, Inc.) were used to create arrays of eight densities: $\phi = 0.010$, 0.020, 0.031, 0.060, 0.091, 0.15, 0.20 and 0.35 for the velocity measurements and $\phi = 0.010$, 0.031, 0.060, 0.091, 0.15, 0.20, 0.27 and 0.35 for the tracer study. All arrays, except for the $\phi = 0.031$ arrays, were created in custom-made 71.1 cm × 40.0 cm perforated polyvinyl chloride (PVC) sheets of either 20% or 35% hole fraction. The locations of the holes in these sheets were defined by generating uniformly distributed random coordinates for the hole centres until the desired number of non-overlapping holes was assigned; these non-overlapping holes were drilled into the sheets. Here, "non-overlapping" holes were defined to have no other hole centre fall within a $2d \times 2d$ square around their centres. Any directional bias resulting from this definition, instead of defining the overlap over a circle of radius d, is assumed negligible. The $\phi = 0.20$ and 0.35 arrays were created by filling all of the holes. The $\phi = 0.010, 0.020, 0.060, 0.091, 0.15$ and 0.27 arrays were created by selecting the holes to be filled or to be left empty using MATLAB's random number generator. The $\phi = 0.031$ array in the tracer study was created by partially filling 20% hole fraction PVC sheets with 1/2-inch staggered hole centres (Ametco Manufacturing Corporation). The $\phi = 0.031$ array used in the velocity measurements were created by partially filling Plexiglas boards that were designed by White & Nepf (2003). Note that White & Nepf (2003) defined non-overlapping holes to have no other hole centre fall within a concentric circle of diameter $4d$. In the tracer study, the dowels were inserted into four PVC sheets placed along the bed of the working section of the flume. A plan view of a section of the $\phi = 0.27$ array is presented in figure 3. For the velocity measurements, different numbers of PVC sheets were used

ϕ	array base	$d/\langle s_n \rangle_A$	array length [cm]	Δx_{gap} [cm]	n
0.010	PVC	0.28	569.0	0.0	118
0.020	PVC	0.43	497.8	0.0	147
0.031	Plexiglas	0.49	498.8	0.0	261
0.060	PVC	0.93	284.5	0.0	260
0.091	PVC	1.3	284.5	0.7 – 1.3	191
0.15	PVC	2.0	213.4	0.0	195
0.20	PVC	2.7	213.4	0.0, 0.1	136
0.35	PVC	5.9	106.1	0.3, 0.6	116, 22

TABLE 1. Array setup for LDV measurements. Δx_{gap} is the width of the gap that was created in the cylinder array to permit multiple LDV measurements in each lateral transect. $\Delta x_{gap} = 0.0$ indicates an unmodified array. n is the total number of time records collected at $Re_s \equiv U_p s/\nu > 250$ ($\phi = 0.010$–0.20) and both $Re_s > 200$ and $Re_s > 250$ for $\phi = 0.35$.

(see table 1) because the density of cylinders increases with ϕ and a shorter array length is required to achieve fully developed conditions at higher ϕ. The cylinders are perpendicular to the horizontal bed of the working section of the flume.

As stated previously, velocity measurements taken in emergent cylinder arrays by White & Nepf (2003) and in the present study (e.g. figures 7 and 8) have shown that $\langle \overline{u} \rangle$ is approximately constant within the array, except very close to the bed and the sidewalls. Therefore, $\langle \overline{u} \rangle$ is approximated by U_p, measured as the time-averaged volumetric flow rate divided by the width of the working section, $\langle \overline{H} \rangle$ at the measurement location, and $1 - \phi$. Similarly, Reynolds numbers were calculated using U_p as the velocity scale.

3.1. *Velocity measurements*

Velocity measurements were taken in a 670 cm × 20.3 cm × 30.5 cm recirculating Plexiglas laboratory flume using two-dimensional LDV (Dantec Measurement Technology). The time-averaged water depth at the LDV sampling volume ranged from $\langle \overline{H} \rangle = 13.1$ cm to $\langle \overline{H} \rangle = 22.1$ cm. Flow was generated by a centrifugal pump and measured with an in-line flow meter. At each ϕ, time records of longitudinal and vertical velocity components were collected at positions $(s+d)/4$ apart along a lateral transect at several streamwise positions within the array for a range of Re_s. The lateral transects were at an elevation of $2\langle \overline{H} \rangle/3$ from the bed.

In total, 2107 time records were collected. The time average ($\overline{u}$, $\overline{w}$), the temporal deviations (u', w') and the variance ($\overline{u'^2}$, $\overline{w'^2}$) were calculated for each record as

$$\overline{u} = \frac{\sum_k u_k \Delta t_k}{\sum_k \Delta t_k}, \tag{3.1}$$

$$u'_k = u_k - \overline{u} \tag{3.2}$$

and

$$\overline{u'^2} = \frac{\sum_k u'^2_k \Delta t_k}{\sum_k \Delta t_k}, \tag{3.3}$$

respectively, where Δt_k is the residence time of the kth seeding particle in the LDV sampling volume. The vertical components are defined analogously. Note that only $u(t)$ and $w(t)$ could be measured. However, previous measurements indicate $\overline{v'^2} \approx \overline{u'^2}$ (Tanino & Nepf 2007), and the turbulent kinetic energy per unit mass, k_t, was determined as $k_t = (2\overline{u'^2} + \overline{w'^2})/2$.

The integral length scale l_t can be estimated from the time record of turbulent fluctuations. Specifically, $|\overline{u}|/(2\pi f_{peak,v_j})$, where f_{peak,v_j} is the frequency at which the frequency-weighted power spectral density of v'_j peaks, is approximately equal to the Eulerian integral length scale (Kaimal & Finnigan 1994, p. 38) and is one measure of l_t (e.g. Pearson, Krogstad & van de Water 2002). To determine f_{peak,v_j}, $u'(t)$ and $w'(t)$ records were resampled at uniform time intervals by linear interpolation. The shortest interval between consecutive samples in that time record was used as the interval. The power spectral densities [cm^2 s^{-2} Hz^{-1}] of the reevaluated $u'(t)$ and $w'(t)$ were determined using MATLAB's pwelch.m function. A peak at 120 Hz exists in most records, which is attributed to background noise. Because this frequency is one order of magnitude higher than the maximum U_p/d and U_p/s in our experiments, which were 15 Hz and 30 Hz, respectively, it is assumed that this noise did not interfere with the analysis. Also, the resampled record is accurate only to $f = \overline{f_{raw}}/(2\pi)$, where $\overline{f_{raw}}$ is the mean data rate of the raw time record (Tummers & Passchier 2001). Accordingly, frequencies above $\overline{f_{raw}}$ and 110 Hz were neglected in the analysis. Finally, l_t was estimated from the frequency $f_{peak,u}$ corresponding to the peak in the frequency-weighted power spectral density of the resampled $u'(t)$ as

$$l_{peak,u} \equiv \frac{|\overline{u}|}{2\pi f_{peak,u}}. \tag{3.4}$$

The vertical length scale, $l_{peak,w}$, was determined from the power spectral density of w' analogously. Of a total of 1317 $l_{peak,u}$ measurements at $Re_s \geqslant 250$, ten were discarded because they differed from the mean $l_{peak,u}$ for that ϕ by more than three standard deviations and three were discarded because a peak could not be identified in the frequency-weighted spectrum.

Alternatively, l_t can be estimated from the autocorrelation function of the local velocity fluctuation as

$$l_{corr,u} \equiv |\overline{u}| \int_0^{\tau_0} \frac{\overline{u'(t)u'(t+\tau)}}{\overline{u'^2}} \, \mathrm{d}\tau, \tag{3.5}$$

where τ is the time lag with respect to t and τ_0 is τ at the first zero-crossing. MATLAB's xcov.m function was used to calculate the variance-normalized autocorrelation function of each resampled $u'(t)$ record, from which the Eulerian integral length scale $l_{corr,u}$ (3.5) was calculated. Of a total of 1290 time records at $Re_s \geqslant 250$ for which $l_{corr,u}$ could be computed, 22 were discarded because the calculated $l_{corr,u}$ deviated from the mean for that ϕ by more than three standard deviations.

The spatial heterogeneity of the velocity field is quantified by the variance of $\overline{u}'' = \overline{u(t)} - U_p$ (e.g. White & Nepf 2003),

$$\frac{\sigma^2_{\overline{u}''}}{U_p^2} = \left\langle \frac{\overline{u}''^2}{U_p^2} \right\rangle - \left\langle \frac{\overline{u}''}{U_p} \right\rangle^2. \tag{3.6}$$

Specifically, measurements of $\overline{u}$ for each ϕ were separated into five or six groups based on U_p. For each (ϕ, U_p) group, $\sigma^2_{\overline{u}''}/U_p^2$ and the maximum and minimum Re_d were computed.

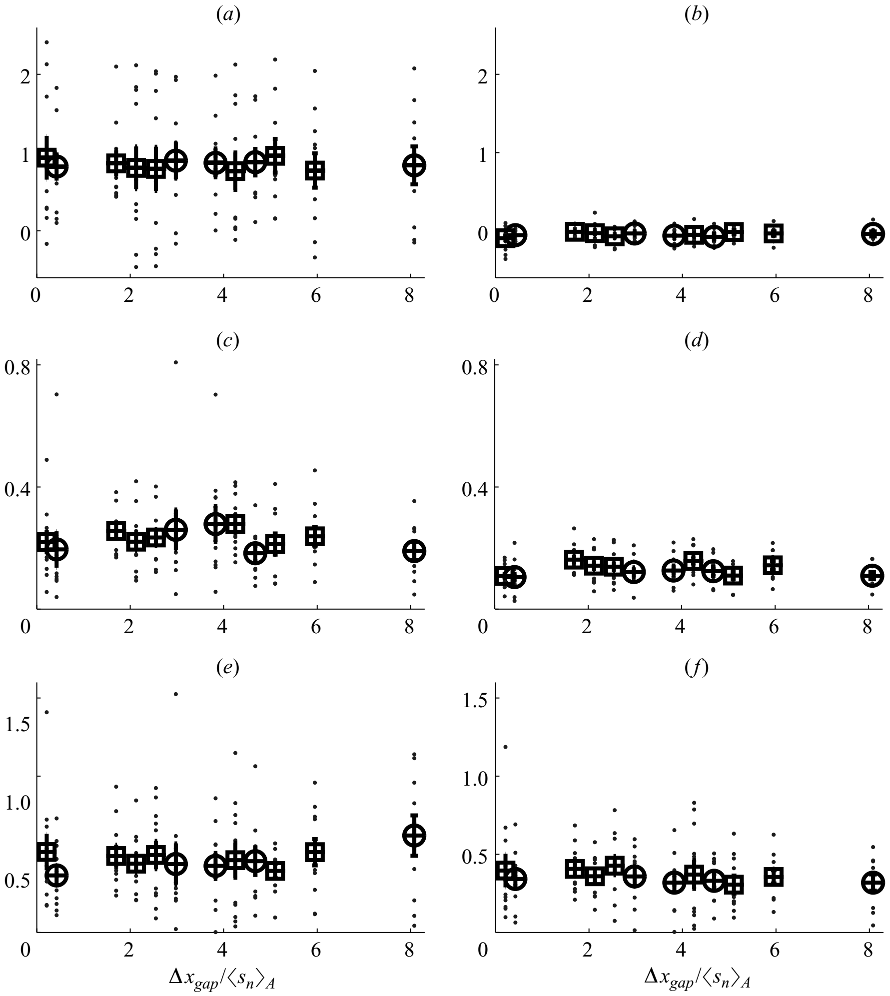

FIGURE 4. Sensitivity of (*a*) $\langle\overline{u}/U_p\rangle$, (*b*) $\langle\overline{w}/U_p\rangle$, (*c*) $\langle\overline{u'^2}/U_p^2\rangle$, (*d*) $\langle\overline{w'^2}/U_p^2\rangle$, (*e*) $\langle l_{peak,u}\rangle/d$ and (*f*) $\langle l_{peak,w}\rangle/d$, as defined by (3.1)–(3.4), to Δx_{gap}, the width of the gap in the array at the sampling locations. Ten or eleven time records were collected at lateral intervals of $(s+d)/2$ along a single lateral transect in a $\phi=0.20$ array for each Δx_{gap}. Dots represent the local values and open markers represent the lateral average over each transect. $Re_s=430$–480 (circle) and $Re_s=470$–540 (square). Vertical bars indicate the standard error of the mean.

Except in the sparsest arrays, measurements could not be collected across the entire width of the flume because cylinders obstructed the LDV laser beams. To permit sufficient sampling positions along each transect, gaps of normalized width $\Delta x_{gap}/\langle s_n\rangle_A=1.4$–$2.7$, 0.0–0.4 and 3–6 were created in arrays of $\phi=0.091$, 0.20 and 0.35, respectively (table 1). To determine whether these gaps biased the results, velocity time records were collected along a lateral transect in a $\phi=0.20$ array for a range of Δx_{gap}, from which lateral averages of $\overline{u}/U_p$, $\overline{w}/U_p$, $\overline{u'^2}/U_p^2$, $\overline{w'^2}/U_p^2$, $l_{peak,u}/d$ and $l_{peak,w}/d$ were calculated for each transect. The lateral averages, with the exception of $\langle\overline{w}/U_p\rangle$ and $\langle\overline{w'^2}/U_p^2\rangle$, remained within standard error of their respective values at $\Delta x_{gap}/\langle s_n\rangle_A=0.2$ in the range $\Delta x_{gap}/\langle s_n\rangle_A=0.2$ to 8.1 ± 0.4 (figure 4). The constant values suggest that our results were not biased by the gaps.

The duration of measurement at a single position was determined from the time taken for the time average and the variance, as defined by (3.1)–(3.3), of preliminary velocity time records to converge to within 5% of their 20-minute average. This test was performed for each ϕ for several Re_d. The duration varied from 60 s to 1000 s, with lower Re_d generally requiring a longer time to converge.

3.2. *Tracer experiments*

Laser-induced fluorescence (LIF) was used to measure the lateral dispersion coefficient in a recirculating Plexiglas laboratory flume with a 284 cm × 40 cm × 43 cm working section. LIF measurements could not be collected in the same flume as the LDV measurements because the seeding material used in the latter would have interfered with the former. The use of the two flumes is justified because the spatially averaged turbulence characteristics are determined by the macroscopic array properties and are not specific to the flume system, as demonstrated by the good agreement in mean turbulence intensity and $l_{peak,u}/d$ observed by White (2002) and in the present study (figures 12 and 15).

Dilute rhodamine WT was injected continuously from a horizontal needle with a syringe pump (Orion Sage^{TM} M362) at a rate that was matched visually with the local flow. A single horizontal beam of argon ion laser (Coherent INNOVA^{R} 70 ion laser) passed laterally through the flume at a single streamwise position x downstream of the tracer source. A Sony CCD Firewire digital camera XCD-X710 controlled by Unibrain Fire-i 3.0 application captured the line of fluoresced tracer from above the flume in a sequence of 1024×48 bitmap images. To filter out the laser beam, 530 nm and 515 nm long-pass filters (Midwest Optical Systems, Inc.) were attached to the camera. The fluorescence intensity is proportional to the rhodamine WT concentration. The correct spatial scale on the images was determined from a photo of a ruler submerged horizontally in the position of the laser beam. The image of the ruler was taken every time the local water depth, the camera setting or the position of the laser beam or the camera changed. At high ϕ, cylinders were removed to create the 1.3-cm gap in the array necessary to insert this ruler. This gap also ensured that the laser beam could pass through the entire width of the flume. The position of the laser beam relative to the tracer source, which was restricted by the distance at which the tracer reached the sidewalls, ranged from $x = 5$ cm to $x = 143$ cm. The time-averaged water depth at the longitudinal position of the laser beam ranged from $\langle\overline{H}\rangle = 9.1$ cm to $\langle\overline{H}\rangle = 18.6$ cm. Additional details of the experimental procedure are provided in Tanino & Nepf (2007).

Instantaneous intensity profiles were extracted from the bitmap images, corrected for background and anomalous pixel intensities and averaged over the duration of the experiment to yield a time-averaged intensity profile, $\overline{I(y,t)}$. The time-averaged profile was corrected for noise and background. Then, its variance was calculated as

$$\sigma^2(x) = \frac{M_2(x)}{M_0(x)} - \left[\frac{M_1(x)}{M_0(x)}\right]^2, \tag{3.7}$$

where $M_j(x)$ is the jth moment,

$$M_j(x) = \int_{\kappa_2}^{\kappa_1} y^j \overline{I(y,t)}\, \mathrm{d}y. \tag{3.8}$$

The zeroth, first and second moments and the corresponding σ were calculated by setting the limits of integration in (3.8), $\kappa_{1,2}$, at the two edges of the images. Next, $\kappa_{1,2}$ were redefined as $\kappa_{1,2} = (M_1/M_0) \pm 3\sigma$ and the calculation was repeated. These limits were applied to prevent small fluctuations at large distances from the centre of mass from altering the variance estimate dramatically.

Previous evaluation of the experimental data determined that, within the range of x considered in the present experiments, σ^2 at constant x increases with pore Reynolds number until $Re_s \approx 250$ and is constant at higher Re_s (Tanino & Nepf 2007, figure 4). In this study, we focus on $Re_s > 250$. The net lateral dispersion coefficient normalized by U_p and d for each ϕ was calculated as

$$\frac{K_{yy}}{U_p d} = \frac{1}{2d}\frac{\mathrm{d}\sigma^2}{\mathrm{d}x}, \tag{3.9}$$

where $\mathrm{d}\sigma^2/\mathrm{d}x$ is the gradient of the line of regression applied to all σ^2 measurements at $Re_s > 200$ for $\phi = 0.35$ and at $Re_s > 250$ for all other ϕ. The criterion for $\phi = 0.35$ is lower because the experimental setup could not accommodate the large longitudinal free surface gradient that results from the cylinder drag (Tanino & Nepf 2008) at $Re_s > 250$.

$\langle\sqrt{k_t}/U_p\rangle$ and $K_{yy}/(U_p d)$ at each ϕ were calculated as the gradient of the line of regression of $\sqrt{k_t}$ on U_p and of σ^2 on x normalized by $2d$, respectively. The uncertainty in the gradient of each line of regression was estimated according to Taylor (1997, chapter 8). Consider the line $y = B_0 + B_1 x$ that best fits n data points (x_k, y_k), $k = 1, 2, \ldots, n$ in the least-squares sense. The uncertainty in B_1 is defined as (Taylor 1997, equations 8.12, 8.15, 8.17)

$$\sqrt{\frac{1}{n-2}\sum_{k=1}^{n}\left[y_k - (B_0 + B_1 x_k)\right]^2}\ \sqrt{\frac{n}{n\sum_{k=1}^{n} x_k^2 - \left(\sum_{k=1}^{n} x_k\right)^2}}. \tag{3.10}$$

The uncertainties in $\langle\sqrt{k_t}/U_p\rangle$ and $\mathrm{d}\sigma^2/\mathrm{d}x$ are calculated as (3.10). The uncertainty in $K_{yy}/(U_p d)$ is simply the uncertainty in $\mathrm{d}\sigma^2/\mathrm{d}x$ divided by $2d$.

4. Experimental results

4.1. *Flow visualization*

We first consider the qualitative Reynolds number dependence. Figures 5 and 6 present unprocessed still photos taken in the $\phi = 0.010$ and 0.15 arrays, respectively, at four different Re_d. Recall from § 2 that Re_d is the Reynolds number based on d instead of s, i.e. $Re_d = Re_s d/s$. In figure 5, fluorescein solution was injected approximately 3.7 cm upstream of cylinder A. The injection point is visible at the top of the images in figure 6. The tracer emerges from the needle as a single distinct filament for all Re_d. In figure 6(*a*), the tracer is deflected by the cylinders and is advected through the array forming a streakline that is stationary in time. The flow is unsteady for all other conditions presented in figures 5 and 6 and, consequently, the angle at which the tracer encounters cylinders A and B in figure 5 and cylinder A in figure 6 varies with time. In both arrays, the Re_d dependence is qualitatively the same. The tracer forms distinct, thin ($\ll d$) bands of dyed and undyed fluid at $Re_d \approx 30$ (figures 5*a* and 6*a*). At higher Re_d, turbulent eddies rapidly mix the fluid within the pores, resulting in a more spatially uniform distribution. For example, distinct filaments cannot be distinguished at the bottom of the image in figures 5(*d*) and 6(*d*).

The $\phi = 0.010$ array is sufficiently sparse that individual vortex streets and their interactions can be identified. A laminar vortex street is seen behind cylinder B at

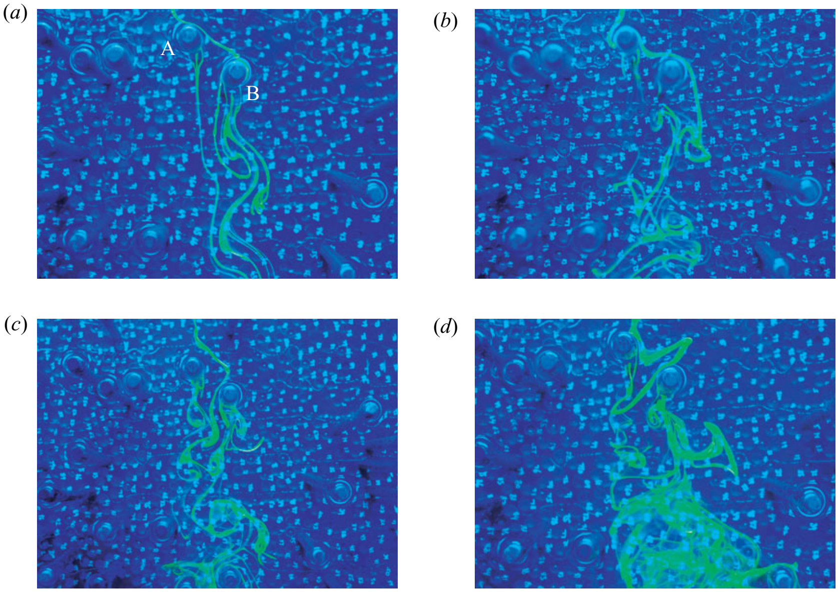

FIGURE 5. Flow visualization by fluorescein and blue lighting in a $\phi = 0.010$ array at the following values of Re_d: (*a*) 28 ± 1, (*b*) 56 ± 3, (*c*) 78 ± 3 and (*d*) 113 ± 5. These values correspond to $Re_s = 220 \pm 10$, 430 ± 20, 600 ± 20 and 880 ± 40, respectively. Mean flow is from top to bottom. Camera and dye injection position were fixed. The injection point is approximately 3.7 cm upstream of cylinder A.

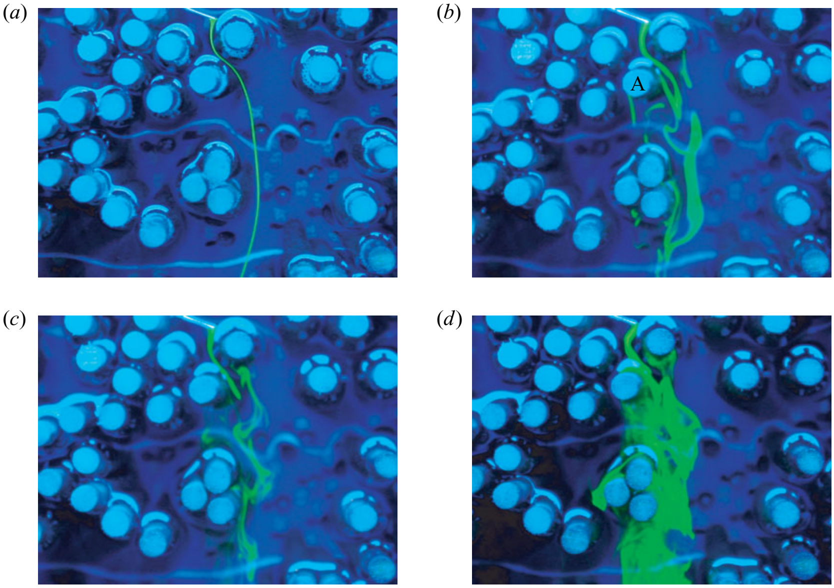

FIGURE 6. Flow visualization by fluorescein and blue lighting in a $\phi = 0.15$ array at the following values of Re_d: (*a*) 32 ± 2, (*b*) 73 ± 3, (*c*) 108 ± 4 and (*d*) 186 ± 7. These values correspond to $Re_s =$ 42 ± 2, 94 ± 4, 139 ± 6 and 240 ± 9, respectively. Mean flow is from top to bottom. Camera and dye injection position were fixed.

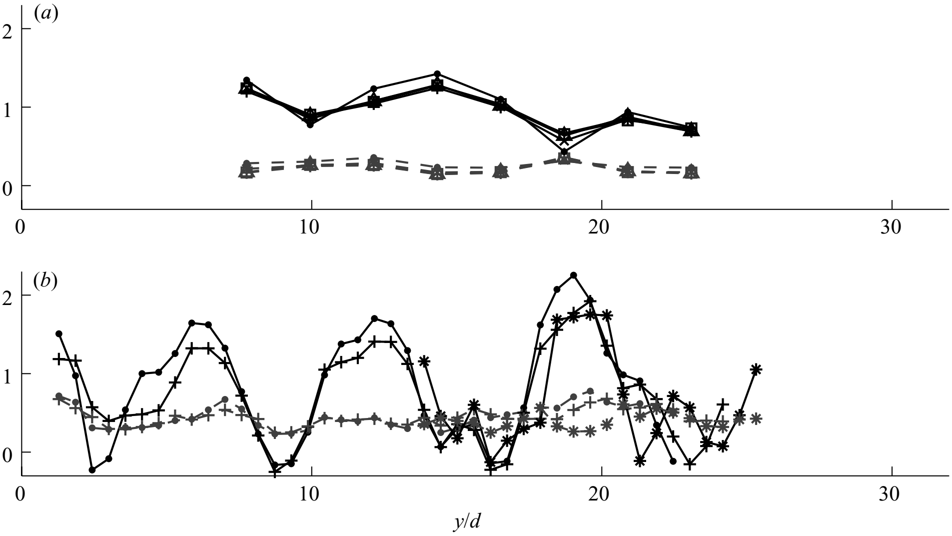

FIGURE 7. Lateral transects of $\overline{u}/U_p$ (solid line) and $\sqrt{k_t}/U_p$ (grey, dashed line) at (*a*) $\phi = 0.010$, $Re_s = 620$–690 (dot), 1600–1700 (×), 2400–2600 (△), 2700–2900 (square), and 3100–3300 (+) and at (*b*) $\phi = 0.15$, $Re_s = 130$–140 (dot), 400–430 (+), and 510–600 (∗). Flume sidewalls were at $y = 0$ and $32.0d$.

$Re_d = 28 \pm 1$ (figure 5*a*). In contrast, a pair of standing eddies are attached to cylinder A in the same image. Here, tracer emerges $O(d)$ downstream of the cylinder as a single, straight filament. The difference between the wakes of cylinders A and B can be attributed to differences in the local flow conditions due to the random nature of the cylinder distribution. At an isolated cylinder, standing eddies form at $Re_d \approx 5$ and become unsteady at $Re_d \approx 40$ (Lienhard 1966). In figure 5(*a*), $Re_d = 28 \pm 1$, and an isolated wake is expected to be steady. The presence of neighbouring cylinders may have elevated the local Re_d such that flow around cylinder B enters the unsteady regime. Figure 5(*a*) also highlights the interaction of the wakes. The single tracer filament leaving cylinder A is drawn into the vortex street of cylinder B as it propagates downstream. At $Re_d = 78 \pm 3$, cylinders A and B both shed vortices (figure 5*c*). Moreover, the shedding is in phase, indicating wake interaction. Here, the centre-to-centre distance between cylinders A and B is approximately $4d$, and the occurrence of wake interaction is consistent with (2.20). The vortex street from the two cylinders appears to merge and form a single turbulent street at approximately $x \approx 15d$. This is consistent with Williamson (1985)'s observations of in-phase vortex shedding behind a pair of side-by-side cylinders. A similar merging of vortex streets can be identified downstream of four cylinders in a square configuration at a 45° angle to the flow (Lam, Li, Chan & So 2003, figure 9, $Re_d = 200$).

4.2. *Velocity and turbulence structure*

Local velocity varies dramatically in the horizontal plane due to the random configuration of the cylinders. This is highlighted in figure 7, in which each subplot presents lateral transects of time-averaged and turbulent components of velocity at a single longitudinal position. For example, the time average of the longitudinal component of velocity ($\overline{u}$) deviates dramatically from its cross-sectional average (U_p) at all ϕ and Re_s. Indeed, $\overline{u}$ is negative at certain positions in the array because of recirculation zones that develop immediately downstream of a cylinder (figure 7*b*).

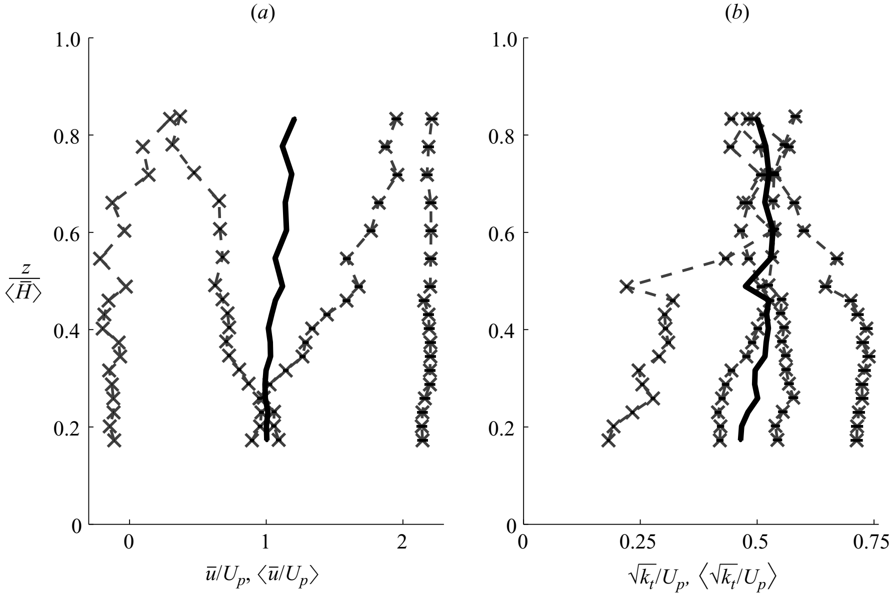

FIGURE 8. Vertical profiles of (a) $\overline{u}/U_p$ and (b) $\sqrt{k_t}/U_p$ at four positions, 1.0d apart, along a lateral transect (×). The lateral average of the four profiles is presented as a thick solid line. Horizontal bars reflect the uncertainty in U_p. $\phi = 0.20$, $Re_s = 440$–490, $\langle \overline{H} \rangle = 17.3$–$17.4$ cm.

A comparison of lateral profiles at different Re_s at the same position in the array indicates that the shape of the lateral profiles remains constant as Re_s varies (figure 7), confirming that the spatial variability is largely dictated by the cylinder configuration. Because the array is vertically uniform, vertical variations in the time-averaged velocity and turbulence intensity are expected to be smaller than their lateral heterogeneity. In particular, spatial averages $\langle \overline{u}/U_p \rangle$ and $\langle \sqrt{k_t}/U_p \rangle$ are approximately uniform in depth (solid lines in figure 8). Similar observations were made in random arrays of $\phi = 0.010$, 0.020 and 0.063 by White & Nepf (2003). Finally, note that the spatial variability is smaller in figure 7(a) ($\phi = 0.010$) than in figure 7(b) ($\phi = 0.15$). Indeed, $\sigma^2_{\overline{u}''}/U_p^2$ increases with ϕ, as illustrated in figure 9 for mean $Re_d = 340$–440.

Like $\overline{u}$ and $\sqrt{k_t}$, the power spectrum and the autocorrelation function vary dramatically in the horizontal plane. The frequency-weighted power spectral density and the autocorrelation function of selected $u'(t)$ records are presented in figure 10 for reference.

The two methods for estimating the integral length scale yield similar values, as expected (figure 11). Therefore, only $\langle l_{peak,u}/d \rangle$ is compared with l_t here (figure 12). The measured integral length scale generally decreases with increasing $d/\langle s_n \rangle_A$, as demonstrated by $\langle l_{peak,u}/d \rangle$, where the spatial average was calculated as the mean of all LDV measurements at $Re_s \geqslant 250$ at each ϕ. Equation (2.13) captures this decrease of $\langle l_{peak,u}/d \rangle$ reasonably well for $d/\langle s_n \rangle_A \geqslant 1.3$. As expected from (2.13), the mean of $\langle l_{peak,u}/d \rangle$ for $d/\langle s_n \rangle_A < 0.5$ is 1.0. However, $\langle l_{peak,u}/d \rangle$ decreases with increasing $d/\langle s_n \rangle_A$ below $d/\langle s_n \rangle_A = 1$ in both the present study and in White (2002)'s experiments. Additional measurements are necessary to verify (2.13) for $d/\langle s_n \rangle_A < 1$.

The mean turbulence intensity at a given ϕ, $\langle \sqrt{k_t}/U_p \rangle$, is calculated as the gradient of the line of regression of all LDV measurements of $\sqrt{k_t}$ on U_p for $Re_s > 250$ at $\phi < 0.35$ and for $Re_s > 200$ at $\phi = 0.35$. The Re_s ranges match those for which

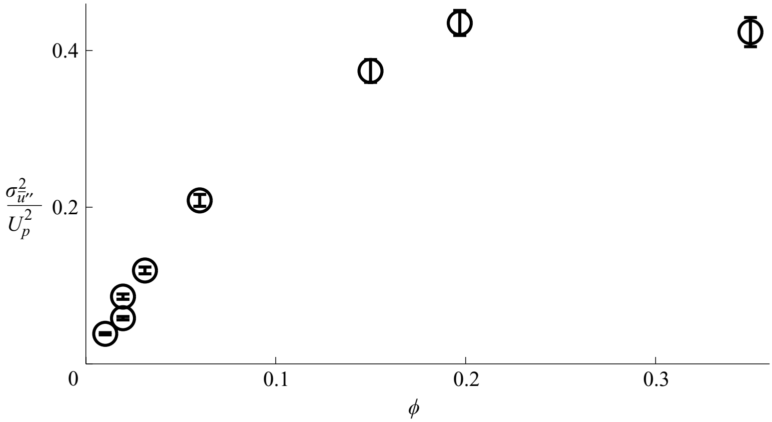

FIGURE 9. Normalized spatial variance of $\overline{u}''$, $\sigma^2_{\overline{u}''}/U_p^2$, for mean $Re_d = 340$–440: (ϕ, Re_d) = (0.010, 410), (0.020, 360), (0.020, 410), (0.031, 390), (0.060, 390), (0.15, 340), (0.20, 430), and (0.35, 430). Two sets of $\sigma^2_{\overline{u}''}/U_p^2$ were calculated from (3.6): one using the upper estimates of U_p and the other using the lower estimates. The ends of the vertical bars reflect these two estimates; the marker is their mean.

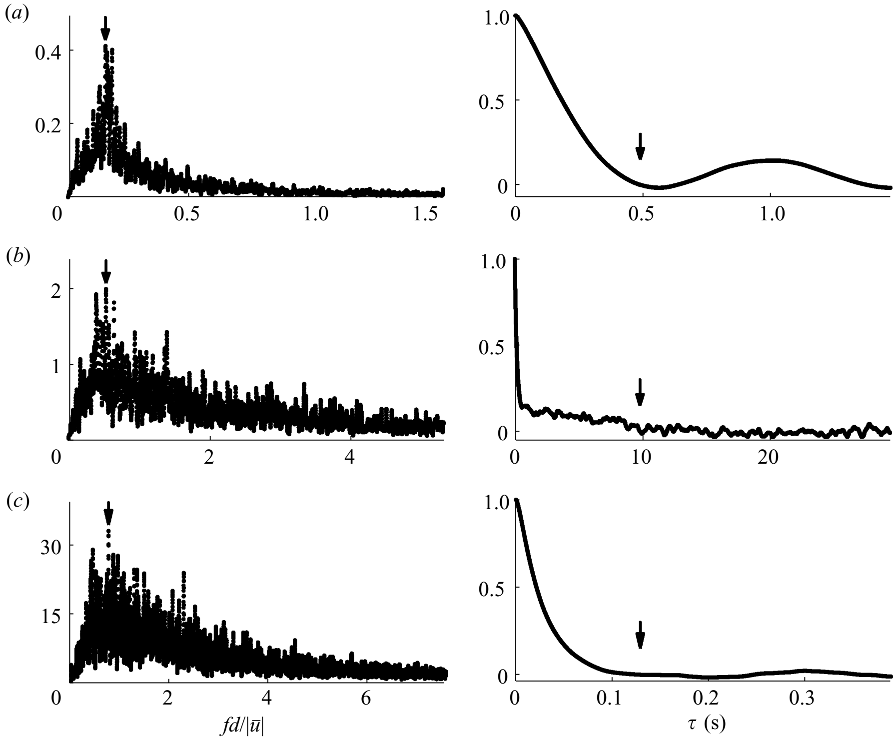

FIGURE 10. The frequency-weighted power spectral density (cm^2 s^{-2}) (left) and the variance-normalized autocorrelation function (right) of selected u' time records: (*a*) $\phi = 0.010$, $\overline{u} = 3.8\,\text{cm s}^{-1}$, $Re_s = 2700$, (*b*) $\phi = 0.20$, $\overline{u} = -1.4\,\text{cm s}^{-1}$, $Re_s = 320$ and (*c*) $\phi = 0.35$, $\overline{u} = 4.9\,\text{cm s}^{-1}$, $Re_s = 380$. Arrows mark the identified peak in the frequency-weighted power spectral density (left) and τ_0 (right). f denotes frequency.

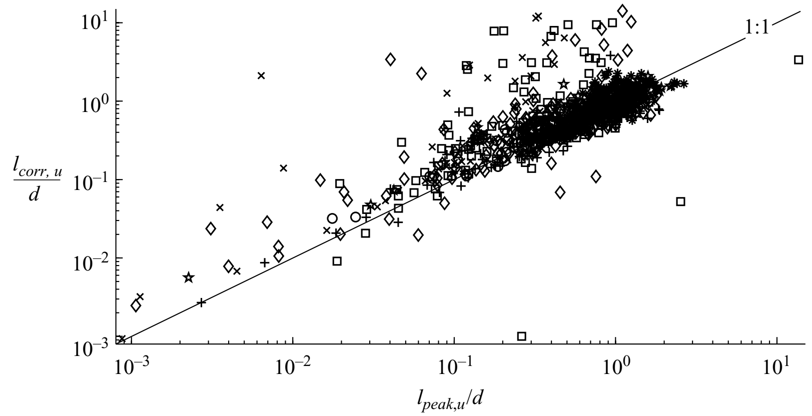

FIGURE 11. Comparison of $l_{peak,u}$ (3.4) and $l_{corr,u}$ (3.5) determined from LDV measurements at $Re_s \geqslant 250$ and $\phi = 0.010$ ($*$), 0.020 (star), 0.031 ($\cdot$), 0.060 ($\diamond$), 0.091 ($+$), 0.15 (square), 0.20 ($\times$), and 0.35 (circle).

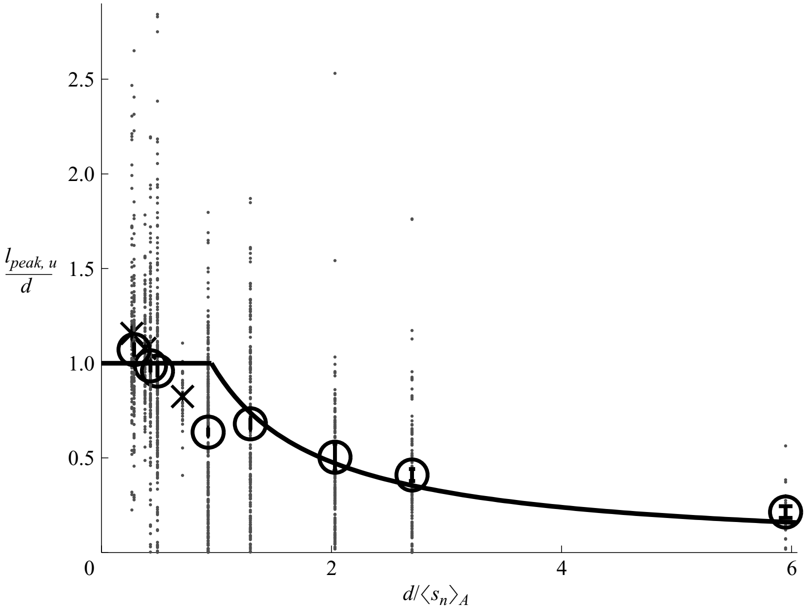

FIGURE 12. $l_{peak,u}/d$ as defined by (3.4) (dots) for LDV measurements at $Re_s \geqslant 250$. Circles mark the mean and vertical bars represent the standard error of the data from the present study for each ϕ. The solid line is (2.13). There are data points at $(d/\langle s_n \rangle_A, l_{peak,u}/d) = (0.49, 5.34)$ and (2.0, 13.6) which are not visible in the figure but are included in the calculation of the mean. White (2002)'s ADV measurements for $Re_s \geqslant 250$ are also included (dots) with their mean ($\times$) and standard error (power spectral density data provided by B. L. White, personal comm.).

$K_{yy}/(U_p d)$ is calculated, as discussed in § 3.2. The observed correlation is highly significant for all ϕ (table 2), indicating that $\langle \sqrt{k_t}/U_p \rangle$ is independent of Re_s under these conditions. The $\sqrt{k_t}$ measurements and the corresponding line of best fit for $\phi = 0.020$ and 0.35 are presented as examples in figure 13. Despite the large

ϕ	Line of regression of $\sqrt{k_t}$ on U_p	R	n
0.010	$(0.07 \pm 0.06) + (0.21 \pm 0.02)U_p$	0.77	118
0.020	$(0.06 \pm 0.04) + (0.26 \pm 0.01)U_p$	0.88	147
0.031	$(0.02 \pm 0.05) + (0.30 \pm 0.01)U_p$	0.81	261
0.060	$(-0.0 \pm 0.1) + (0.38 \pm 0.02)U_p$	0.73	260
0.091	$(0.1 \pm 0.1) + (0.37 \pm 0.02)U_p$	0.80	191
0.15	$(0.0 \pm 0.3) + (0.43 \pm 0.05)U_p$	0.53	195
0.20	$(0.3 \pm 0.5) + (0.47 \pm 0.09)U_p$	0.43	136
0.35	$(0.4 \pm 0.7) + (0.52 \pm 0.10)U_p$	0.44	116

TABLE 2. The equation of the least-squares fit to data at mean $Re_s > 250$ ($\phi = 0.010$–0.20) or at mean $Re_s > 200$ ($\phi = 0.35$). R is the correlation coefficient and n is the total number of data points included in the regression. See table 1 for the corresponding $d/\langle s_n \rangle_A$.

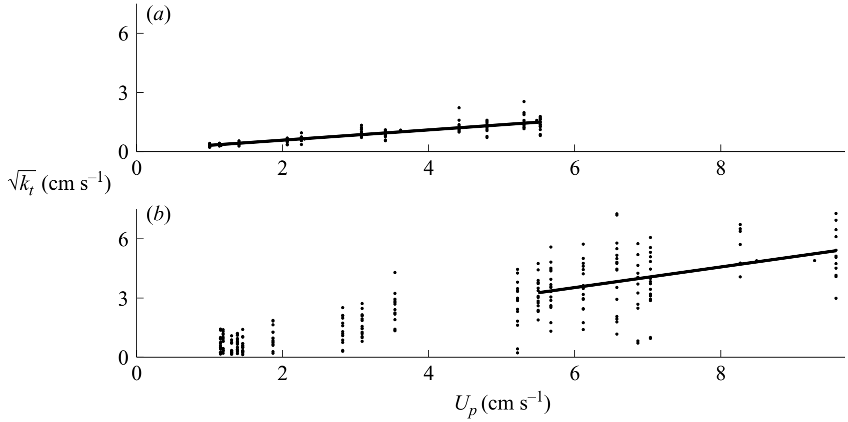

FIGURE 13. All LDV measurements of $\sqrt{k_t}$ for $\phi = (a)$ 0.020 and (b) 0.35. Each dot represents a single time record at one location within the array and the associated U_p. The solid line in each subplot is the least-squares fit to all data in the range (a) $Re_s > 250$ and (b) $Re_s > 200$. See table 2 for the equations for the fitted lines.

spatial heterogeneity in individual (local) $\sqrt{k_t}/U_p$ estimates, their spatial average increases monotonically with ϕ, within uncertainty (figure 14).

The scaling constants for the turbulence intensity scale (2.12) were determined by least-squares fitting (2.12), with l_t defined by (2.13), to the $\langle \sqrt{k_t}/U_p \rangle$ measurements presented in figure 14. The data point at $d/\langle s_n \rangle_A = 0.93$ was excluded from the fitting because it is near the expected transition in l_t, i.e. $d/\langle s_n \rangle_A = 1$. Farther, to avoid discontinuities in the model predictions, we will assume that the transition between the two regimes occurs at $d/\langle s_n \rangle_A = 0.56$, where the two functions intersect, i.e.

$$\left\langle \frac{\sqrt{k_t}}{U_p} \right\rangle = \begin{cases} 1.1 \left[C_D^{form} \dfrac{\phi}{(1-\phi)\pi/2} \right]^{1/3}, & d/\langle s_n \rangle_A < 0.56 \\ 0.88 \left[C_D^{form} \dfrac{\langle s_n \rangle_A}{d} \dfrac{\phi}{(1-\phi)\pi/2} \right]^{1/3}, & d/\langle s_n \rangle_A \geqslant 0.56 \end{cases}, \tag{4.1}$$

where C_D^{form} is described by (2.10). The theory accurately captures the ϕ dependence of the measured $\langle \sqrt{k_t}/U_p \rangle$ for both $d/\langle s_n \rangle_A < 0.49$ and $\geqslant 1.3$ (figure 14). Note that the measurement at $d/\langle s_n \rangle_A = 0.93$ falls between the extrapolation of the two expressions in (4.1), suggesting transition effects.

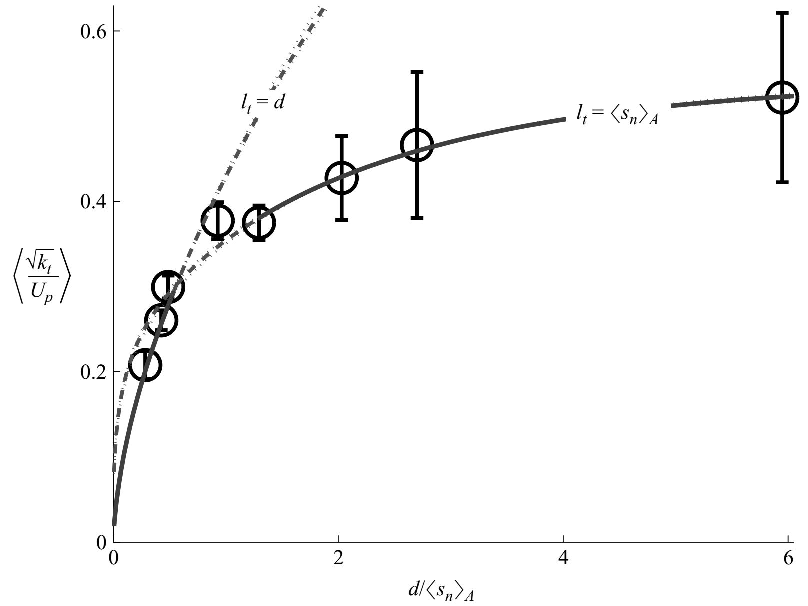

FIGURE 14. The gradient of the line of regression of $\sqrt{k_t}$ on U_p at $Re_s > 250$ for $\phi < 0.35$ and $Re_s > 200$ for $\phi = 0.35$ from the present study only. Vertical bars represent the uncertainty in the gradient as defined by (3.10). Solid lines are (4.1); the empirical fits are extrapolated over the range of the data set (dashed). Dotted lines reflect the uncertainty in C_D^{form}: the lines are (2.12) with the upper and lower estimates of C_D^{form} in (2.10) and the corresponding best-fit scaling constants 0.84 and 0.94 for $l_t = \langle s_n \rangle_A$ and 1.0 and 1.2 for $l_t = d$, respectively.

Field measurements by Neumeier & Amos (2006), Nikora (2000) and Leonard & Luther (1995), presented in figure 15, fall within the range of $\sqrt{k_t}/U_p$ observed in the present study. To the authors' knowledge, these are the only field reports in which both turbulence measurements and stem density are presented for emergent plant canopies. The $\langle \sqrt{k_t}/U_p \rangle$ calculated from White (2002)'s three-dimensional acoustic Doppler velocimeter (ADV) measurements are also presented in figure 15 for comparison. The good agreement between (4.1) and laboratory data suggests that mean turbulence intensity at high Re_s can be predicted in random cylinder arrays from $d/\langle s_n \rangle_A$, ϕ, and C_D^{form}.

4.3. *Net lateral dispersion*

The assumption that net lateral dispersion is Fickian is confirmed by the linear increase of σ^2 with x observed at all ϕ (e.g. figure 16). In addition, Tanino & Nepf (2007, figure 4) have shown that σ^2 measured at a fixed longitudinal distance from the source becomes independent of Re_s at $Re_s > 250$. Consequently, $d\sigma^2/dx$ is also independent of Re_s at $Re_s > 250$ (e.g. figure 16).

The normalized net lateral dispersion coefficients $K_{yy}/(U_p d)$ are presented in figures 17 and 18 and in table 3. The figures include measurements at $\phi = 0$ reported by Nepf *et al.* (1997, table 1). Three distinct regimes can be identified in the figures. In the sparse array, $K_{yy}/(U_p d)$ increases rapidly as ϕ and $d/\langle s_n \rangle_A$ increase. In the present laboratory study, this regime extends from $d/\langle s_n \rangle_A = 0$ to $d/\langle s_n \rangle_A = 0.58$ ($\phi = 0$–0.031). In the intermediate range, $K_{yy}/(U_p d)$ decreases as ϕ increases. This regime extends from $d/\langle s_n \rangle_A = 0.58$ to $d/\langle s_n \rangle_A = 2.7$ ($\phi = 0.031$–0.20) in our arrays. Finally, in the

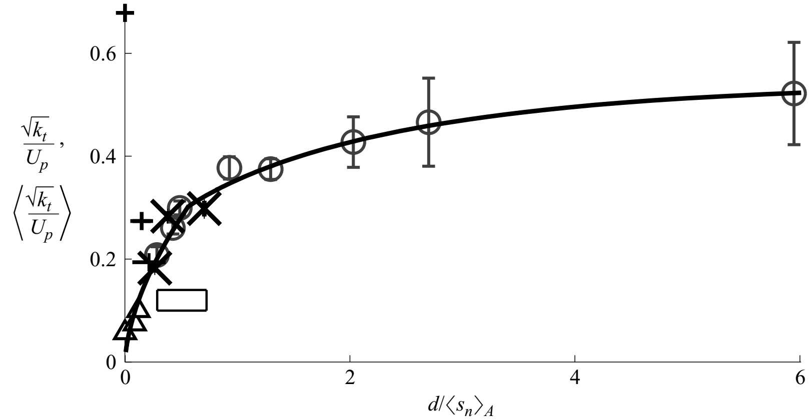

FIGURE 15. $\langle \sqrt{k_t}/U_p \rangle$ calculated from LDV measurements collected in the present study (○) and from White (2002)'s measurements at $\phi = 0.010$, 0.020 and 0.063 (×) (lateral profiles of $\sqrt{\overline{u'^2}}$, $\sqrt{\overline{v'^2}}$, $\sqrt{\overline{w'^2}}$ and $\overline{u}$ were provided by B. L. White, personal comm.). Vertical bars represent the uncertainty in the gradient as defined by (3.10). Field measurements of $\sqrt{k_t}/U_p$ in emergent plant canopies by Nikora (2000, △), Leonard & Luther (1995, +), and Neumeier & Amos (2006, unpublished values and details provided by U. Neumeier, personal comm., rectangle) are also plotted. U. Neumeier provided eight depth profiles of ($\sqrt{\overline{u'^2}}$, $\sqrt{\overline{v'^2}}$, $\sqrt{\overline{w'^2}}$) in emergent canopies, but only the profile where the estimated wind-induced horizontal and vertical wave speeds were less than 50% of the reported r.m.s. speeds (profile $H21$) is included here. The vertical range of the box marks the minimum and maximum values in that profile. The horizontal range in Leonard & Luther (1995) and Neumeier & Amos (2006)'s data represents that in the mean stem d reported in the studies. An exact random distribution was assumed in calculating $\langle s_n \rangle_A$ for the field data from (A 8). Solid line is (4.1).

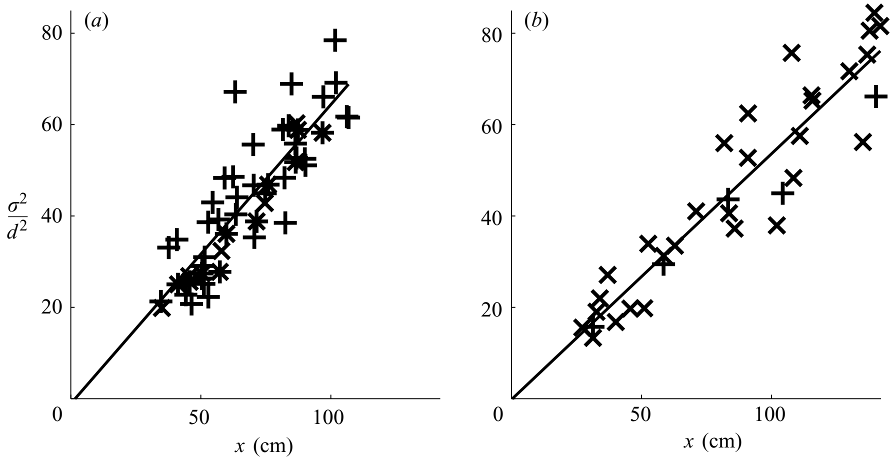

FIGURE 16. $\sigma^2(x)$ for (a) $Re_s = 640$–650 (×), 920–1000 (+), and 1420–1460 (∗) in a $\phi = 0.010$ array and (b) $Re_s = 250$–280 (×) and 480–530 (+) in a $\phi = 0.15$ array. The solid line represents the linear regression on all $Re_s > 250$ data.

densest arrays, $K_{yy}/(U_p d)$ again increases with ϕ, but more gradually. To the authors' knowledge, this ϕ dependence of lateral dispersion over one order of magnitude range of ϕ has not been documented previously.

Nepf *et al.* (1997)'s measurements of $K_{yy}/(U_p d)$ in periodic, staggered cylinder arrays at $Re_s > 2000$ are included in figure 17 (+) for the purpose of qualitative

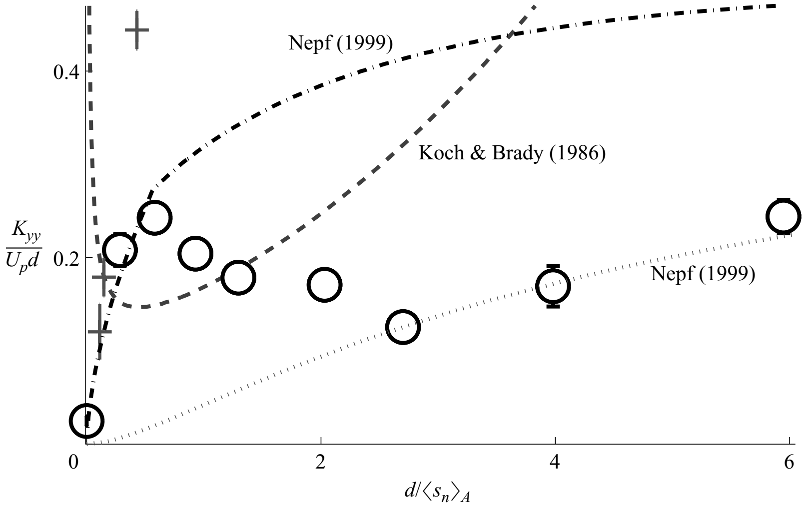

FIGURE 17. Comparison of observed $K_{yy}/(U_p d)$ (○) with (2.4) (dash-dotted), (2.17) (dotted), and (2.18) (dashed); $\langle\sqrt{k_t}/U_p\rangle$ in (2.4) is predicted by (4.1); $\epsilon = d$ in (2.17), as proposed by Nepf (1999); $k_\perp$ in (2.18) is predicted for the arrays used in our experiments as described in Appendix B; $K_{yy}/(U_p d)$ at $\phi = 0$ is taken from Nepf *et al.* 1997, table 1. Also represented are Nepf *et al.* (1997)'s measurements in periodic staggered arrays of $d = 0.6$ cm, $\phi = 0.0046$, 0.014 and 0.055 at $Re_s > 2000$. The marker (+) indicates their mean. For the periodic array, $\langle s_n\rangle_A$ was taken as the minimum distance between cylinders in any direction. Vertical bars on our data represent uncertainty in the gradient of the linear regression of the variance data, as defined by (3.10). Vertical bars on Nepf *et al.* (1997)'s data indicate the quadratic sum of the standard error and the mean of the experimental uncertainty associated with each measurement. Where vertical bars are not visible, they are smaller than the size of the marker.

ϕ	$d/\langle s_n\rangle_A$	n	$K_{yy}/(U_p d)$
0.010	0.28	51	0.21 ± 0.02
0.031	0.58	56	0.24 ± 0.01
0.060	0.93	44	0.20 ± 0.01
0.091	1.3	61	0.18 ± 0.01
0.15	2.0	35	0.17 ± 0.01
0.20	2.7	48	0.13 ± 0.01
0.27	4.0	36	0.17 ± 0.02
0.35	5.9	16	0.24 ± 0.02

TABLE 3. Summary of $K_{yy}/(U_p d)$ data: n is the number of cases for which $Re_s > 250$ ($\phi = 0.010 - 0.27$) and $Re_s > 200$ ($\phi = 0.35$). The uncertainty was calculated as the uncertainty in $d\sigma^2/dx$, defined by (3.10), divided by $2d$.

comparison only. Only measurements for which the exact cylinder configuration is available (see Zavistoski 1994) are presented. It should be noted that Nepf *et al.* (1997)'s measurements do not represent a dispersion phenomenon analogous to the one investigated in the present study. In their experiments, tracer was injected 54 cm upstream of the array (Sullivan 1996). It is not obvious how end effects (i.e. the effects of being transported in non-fully-developed flow) influence the dispersion coefficient.

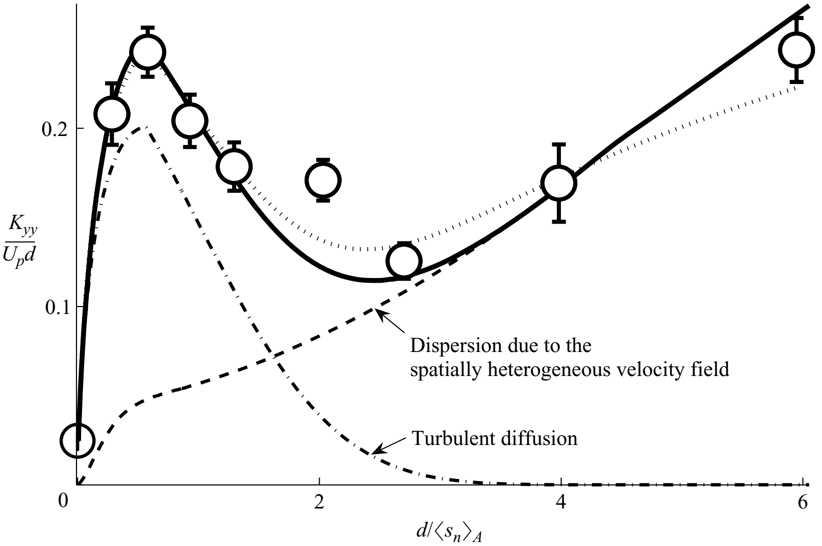

FIGURE 18. Comparison of the observed $K_{yy}/(U_p d)$ (○) with the theory. $K_{yy}/(U_p d)$ at $\phi = 0$ is taken from Nepf *et al.* 1997, table 1. Solid line is (2.21), with scaling constants $\gamma_1 = 4.0$ and $\gamma_2 = 0.34$, as determined from least-squares fitting to data; $\langle \sqrt{k_t}/U_p \rangle$ in (2.21) is predicted by (4.1). The two terms that constitute (2.21) – (2.20) (dashed) and (2.16) (dashed-dotted) – are also presented. The dotted line is the linear superposition of (2.17) and (2.16); $\epsilon = d$ was imposed and the scaling constant $\gamma_1 = 4.5$ was determined from least-squares fitting to data. Vertical bars for $\phi > 0$ represent uncertainty in the gradient of the linear regression of the variance data, as defined by (3.10). The vertical bar on Nepf *et al.* (1997)'s data point ($\phi = 0$) indicates the quadratic sum of the standard error and the mean of the experimental uncertainty associated with each measurement. Where the vertical bars are not visible, they are smaller than the marker.

Also, the nearest-neighbour spacing was anisotropic in Nepf *et al.* (1997)'s arrays, and $\langle s_n \rangle_A$ may not be the appropriate length scale.

Models proposed by Nepf (1999) and Koch & Brady (1986) are compared with experiment in figure 17. Nepf (1999)'s model for turbulent diffusion (2.4) is consistent with the qualitative trend observed in the sparse array regime ($\phi \leqslant 0.031$). However, the model does not capture the decrease in $K_{yy}/(U_p d)$ observed from $d/\langle s_n \rangle_A = 0.58$ to $d/\langle s_n \rangle_A = 2.7$ and, consequently, overpredicts $K_{yy}/(U_p d)$ above $d/\langle s_n \rangle_A = 0.58$. Note that (2.4) is equivalent to assuming that the product of $\langle l_e \rangle_m / d$ and the effective porosity, V_m/V, in (2.15) is constant for all ϕ. Consequently, (2.4) predicts that turbulent diffusion will grow monotonically with $d/\langle s_n \rangle_A$. In contrast, $(\langle l_e \rangle_m / d)(V_m/V)$ decreases monotonically as ϕ increases in our formulation (2.16), which permits a description of turbulent diffusion that decreases with increasing $d/\langle s_n \rangle_A$ for $d/\langle s_n \rangle_A > 0.56$ (dash-dotted line in figure 18).

At high ϕ ($\geqslant$0.20), where physical reasoning suggests that dispersion due to the spatially heterogeneous velocity field is most important, Nepf (1999)'s random walk model (equation 2.17 with $\epsilon = d = 0.64$ cm) yields good quantitative agreement with the data. While Koch & Brady (1986)'s Stokes flow solution (2.18) predicts the correct qualitative trend at $\phi \geqslant 0.20$, the quantitative agreement with the experiment is poor: the solution dramatically overpredicts our measurements at $\phi = 0.20$, 0.27 and 0.35. Also, (2.18) predicts a rapidly increasing contribution as ϕ decreases below $d/\langle s_n \rangle_A = 0.44$ (figure 17). The laboratory data exhibit the opposite trend, with

$K_{yy}/(U_p d)$ decreasing as $d/\langle s_n\rangle_A$ decreases below 0.58. In the proposed modification (2.20), (2.18) is multiplied by $P_{s_{nc}<5d}$, the probability that a single cylinder in the array will have a nearest neighbour within $r=5d$. As ϕ decreases to zero, $P_{s_{nc}<5d}$ monotonically decreases to zero, which also allows (2.20) to remain finite.

The linear superposition of models describing the contributions of turbulence and the spatially heterogeneous velocity field to net dispersion (e.g. equation 2.21; $r^*/d=2$) is compared with experiment in figure 18. Recall that r^* is the minimum centre-to-centre separation between neighbouring cylinders necessary for the fluid between them to contain eddies with mixing length scale $l_e \geqslant d$. Here, we anticipated that $l_e = l_t$ and imposed $r^*/d=2$. The best-fit scaling constants $\gamma_1=4.0$ and $\gamma_2=0.34$ were determined by substituting (4.1) and $r^*/d=2$ into (2.21) and fitting the resulting expression, in the least-squares sense, to the observed $K_{yy}/(U_p d)$ for $\phi>0$. Because the two expressions for dispersion due to the spatially heterogeneous velocity field have a similar dependence on ϕ, replacing (2.20) in (2.21) with (2.17 ($\epsilon=d$)) yields comparable agreement to data (dotted line). The corresponding scaling constant for the turbulent diffusion model is $\gamma_1=4.5$. The proposed model for net dispersion captures the three observed regimes. Some disagreement between theory and experiment occurs at $d/\langle s_n\rangle_A=2.0$ ($\phi=0.15$), suggesting nonlinear interactions between the two components of lateral dispersion at this $d/\langle s_n\rangle_A$. Note that (2.21) suggests that the contribution from the spatially heterogeneous velocity field to net lateral dispersion first exceeds the contribution from turbulent diffusion around this $d/\langle s_n\rangle_A$ ($=1.6$).

The present model for turbulent diffusion suggests that its contribution increases rapidly with $d/\langle s_n\rangle_A$ until $d/\langle s_n\rangle_A=0.56$ and then decays as $d/\langle s_n\rangle_A$ increases farther. With the best-fit scaling constants determined above, the predicted contribution from turbulence constitutes less than 1% of the predicted net $K_{yy}/(U_p d)$ for $d/\langle s_n\rangle_A>3.3$, and the theory suggests that dispersion arises predominantly from the spatial heterogeneity in the velocity field due to the solid obstructions. Note that $P_{s_{nc}<5d}=1$ at $d/\langle s_n\rangle_A>3.3$, and the ϕ dependence predicted by (2.21) is captured entirely by Koch & Brady (1986)'s Stokes flow solution (2.18). The good agreement despite the high Re_s suggests that, at high ϕ, the time-averaged velocity field may not be strongly altered by turbulence, whose length scale is constrained by the cylinder separation. This farther suggests that $K_{yy}/(U_p d)$ may not change significantly from Stokes flow to high $Re_s>250$ at high $d/\langle s_n\rangle_A$. Additional measurements are necessary to verify our assumption of Re_d independence. The same data can be used to examine whether the choice of $\epsilon=d$ in the random walk model (2.17) is appropriate at lower Re_d.

Finally, let us evaluate the assumption $r^*/d=2$ that we imposed to determine the scaling constants γ_1 and γ_2 in (2.21). If r^* is treated as a third fitting parameter, least-squares fitting (2.21) to the experimental data at $\phi>0$ yields $r^*/d=1.6$ ($\gamma_1=3.8$ and $\gamma_2=0.32$), which agrees with $r^*/d=2$ to within 20%, suggesting that $l_e=l_t$ is a reasonable approximation.

5. Conclusions

Laboratory measurements of turbulence and lateral dispersion in random arrays of cylinders of diameter $d=0.64\,\text{cm}$ at $Re_s>250$ were presented for $\phi=0.010$–0.35. In sparse arrays, the characteristic size of the largest turbulent eddies is $l_t=d$. However, when the mean nearest-neighbour cylinder spacing, $\langle s_n\rangle_A$, is smaller than d, the turbulence length scale becomes constrained by the pore size (figure 12). Thus, even though mean turbulence intensity increases monotonically with ϕ (figure 14), its contribution to solute dispersion declines in this regime. Our experiments verified that mean turbulence intensity can be predicted in terms of the cylinder density, l_t/d, and C_D^{form} only. Farther, since C_D^{form} in a random cylinder array is a function only of ϕ for a constant d (Tanino & Nepf 2008), mean turbulence intensity in a random cylinder array can be described as a function of ϕ and d only.

The normalized coefficient for net lateral dispersion $K_{yy}/(U_p d)$ increases, decreases and then increases again as ϕ increases. The observed $K_{yy}/(U_p d)$ is described accurately by a linear superposition of models describing the contributions of turbulence and the spatially heterogeneous velocity field. Comparable agreement is achieved by describing the contribution from the latter by a one-dimensional random walk model with a step size that is comparable to the cylinder diameter, as proposed by Nepf (1999), and by a modification of Koch & Brady (1986)'s Stokes flow solution. The good agreement with the experiment supports the two main assumptions of our turbulent diffusion model. First, only turbulent eddies with characteristic mixing length $l_e \geqslant d$ contribute significantly to net lateral dispersion. Second, neighbouring cylinder centres must be farther than $r^* = 2d$ from each other for the pore space between them to contain such eddies. The fractional volume of the array that comprises pores larger than this critical length scale decreases with increasing $d/\langle s_n \rangle_A$. Consequently, although $\langle \sqrt{k_t}/U_p \rangle$ increases monotonically with $d/\langle s_n \rangle_A$, the contribution of turbulent diffusion to net lateral dispersion decreases for $d/\langle s_n \rangle_A > 0.56$, correctly capturing the observed decrease in net lateral dispersion at intermediate densities.

The conceptual framework presented here is not specific to arrays of circular cylinders. Specifically, the results suggest that the integral length scale l_t and mean turbulence intensity can be determined simply from the distribution and geometry of the elements. In addition, the three $d/\langle s_n \rangle_A$ regimes identified for $K_{yy}/(U_p d)$ are expected to apply to solute transport in random arrays in general. Farthermore, observations of transverse dispersion in ceramic foam agree with Koch & Brady (1985)'s theory for a packed bed of spheres in Stokes flow (e.g. Pereira *et al.* 2005, figure 3*d*). This agreement suggests that, at least in isotropic media of $\phi = O(0.13)$, transverse dispersion is not sensitive to the exact geometry of the individual obstacles (Hackert *et al.* 1996). Similarly, (2.21), with the scaling constants determined in this work, may accurately describe transport in plant canopies of slightly different stem morphology. Finally, the good agreement between the data and the model for the contribution from the spatially heterogeneous velocity field based on Koch & Brady (1986)'s analytical solution at $\phi \geqslant 0.20$ suggests that lateral dispersion predictions based on Stokes flow analysis may be applicable at higher Reynolds numbers at sufficiently high ϕ. Indeed, Hackert *et al.* (1996) and Pereira *et al.* (2005)'s transverse dispersion measurements, which also agree with a Stokes flow solution (discussed above), were collected at pore Reynolds numbers of 10–300, where inertia is clearly non-negligible.

This material is based on work supported by the National Science Foundation grant EAR–0309188. Any opinions, conclusions, or recommendations expressed in this material are those of the authors and do not necessarily reflect the views of the National Science Foundation. The authors thank Brian L. White for providing unpublished ADV measurements from his Master's thesis (White 2002) and Dr Urs Neumeier for providing unpublished velocity measurements from Neumeier & Amos (2006). The authors would also like to thank David Gonzalez-Rodriguez for contributing the approach to deriving the analytical expressions for the nearest-neighbour parameters presented in Appendix A. Finally, we would like to thank the three anonymous reviewers for their comments.

Appendix A. Mean nearest-neighbour distance and related parameters in a random array

Consider an array of N circular holes of diameter d randomly distributed in a board of horizontal area A. The corresponding hole volume fraction is $\phi = (\pi/4)d^2N/A$. This array is created by generating uniformly distributed random coordinates for the hole centres. If a random coordinate is sufficiently far from previously assigned holes, that coordinate is assigned as a hole centre and the appropriate area around it is marked as occupied. The process is repeated until N hole centres are assigned. Let N_c be the number of random coordinates that has to be generated to assign the N hole centres. Then, the total number of generated random coordinates that must be neglected, $N_c - N$, is

$$N_c - N = \sum_{i=1}^{N_c} \frac{(i-1)(N/N_c)A_h}{A}, \tag{A 1}$$

where A_h is the area around a hole centre in which another hole centre cannot be assigned (referred to as the 'invalid' area around a hole centre). Solving for N_c yields

$$\frac{N_c}{N} = \frac{1 - (2\phi/N)A_h/(\pi d^2)}{1 - 2\phi A_h/(\pi d^2)}. \tag{A 2}$$

Theoretically, the invalid area around a hole centre is a circle of radius d. Then, $A_h = \pi d^2$.

The generation of random coordinates within a small region of the array satisfies the two conditions of a Poisson process. First, the expected number of random coordinates generated per unit area is constant at $\lambda > 0$, where

$$\lambda \equiv \frac{N_c}{A} = \frac{\phi}{(\pi/4)d^2}\frac{N_c}{N}. \tag{A 3}$$

Second, the number of hole centres in two non-overlapping areas within a small region of the array can be assumed independent. Then, the number of random coordinates generated in a circular area a has a Poisson distribution with parameter λa (Devore 2000, pp. 136–137). Also, the circular area concentric with a random coordinate and spanning to its nearest random coordinate has an exponential probability distribution function (p.d.f.) (Devore 2000, pp. 174–175).

In the array, each assigned hole occupies a finite circular area of radius $d/2$, and the smallest possible distance between non-overlapping hole centres is d. Then, the p.d.f. of the circular area concentric with a hole centre and spanning to its nearest-neighbour hole centre, A_n, is truncated at $a = A_L$:

$$f(a;\lambda) = \frac{1}{\beta}\begin{cases}\lambda \mathrm{e}^{-\lambda a}, & a \geqslant A_L \\ 0, & a < A_L\end{cases}, \tag{A 4}$$

where

$$\beta = \int_{A_L}^{\infty} \lambda \mathrm{e}^{-\lambda a}\,\mathrm{d}a = \mathrm{e}^{-\lambda A_L} \tag{A 5}$$

and $A_L = \pi d^2$. Although A_L and A_h are equal here, the two parameters are not interchangeable, as will be shown in § A.1. A_L is, by definition of (A 4), a circular

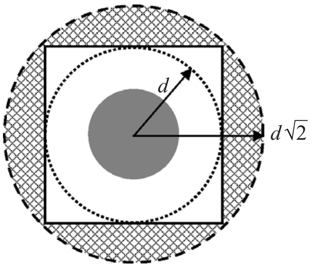

FIGURE 19. Definition of invalid area around an assigned hole centre. Physically, the area invalidated by the finite volume of the hole (solid circle) is the dotted circle, radius d. However, a $2d \times 2d$ square around a hole centre was defined as invalid space in the numerical code used to assign the hole coordinates in the PVC sheets used in the laboratory experiments. The dashed circle marks the circle that circumscribes this square region.

area that defines the smallest a for which $f(a;\lambda)$ is non-zero. In contrast, A_h does not assume a geometry for the invalid area around an assigned hole.

This distribution describes the value measured by taking an array of randomly distributed hole centres, selecting one hole centre, and finding its nearest neighbour and the corresponding A_n. Additional values would be measured by repeating these steps in different independent arrays. This process is different from identifying the nearest neighbour of, and measuring the corresponding A_n for, each hole centre in a single array, where measurements are dependent. While the two random variables have different distributions, their means are the same. Thus, $\int_{-\infty}^{\infty} af(a)\mathrm{d}a$ yields the correct mean radial area $\langle A_n\rangle_A$ to the nearest-neighbouring hole centre. From (A 4) and (A 5), the expected values for the centre-to-centre distance between nearest neighbours, s_{nc}, and s_{nc}^2 are

$$\frac{\langle s_{nc}\rangle_A}{d} = \sqrt{\frac{A_L}{\pi d^2}} + \frac{1-\mathrm{erf}(\sqrt{\lambda A_L})}{2\sqrt{\lambda d^2}\mathrm{e}^{-\lambda A_L}} \tag{A 6}$$

and

$$\frac{\langle s_{nc}^2\rangle_A}{d^2} \equiv \frac{\langle A_n\rangle_A}{\pi d^2} = \frac{A_L}{\pi d^2} + \frac{1}{\lambda\pi d^2}. \tag{A 7}$$

Applying A_L, $A_h = \pi d^2$, (A 2) and (A 3) to (A 6) and (A 7) yields

$$\frac{\langle s_{nc}\rangle_A}{d} \approx 1 + \frac{\sqrt{\pi}}{2}\sqrt{\frac{1-2\phi}{4\phi}}\frac{[1-\mathrm{erf}\left(\sqrt{4\phi/(1-2\phi)}\right)]}{\mathrm{e}^{-4\phi/(1-2\phi)}} \tag{A 8}$$

and

$$\frac{\langle s_{nc}^2\rangle_A}{d^2} \approx \frac{1+2\phi}{4\phi}. \tag{A 9}$$

A.1. *Invalid area defined as a $2d \times 2d$ square*

In creating the PVC sheets used in this study, a $2d$ x $2d$ square circumscribing each assigned hole was invalidated instead of a concentric circle of radius d (figure 19). Here, $A_h = (2d)^2$ instead of $A_h = \pi d^2$, and (A 2) yields

$$\frac{N_c}{N} = \frac{1-2d^2/A}{1-(8/\pi)\phi} \approx \frac{1}{1-(8/\pi)\phi}. \tag{A 10}$$

The corresponding λ is determined by substituting (A 10) into (A 3).

The p.d.f. is $f(a;\lambda)=0$ in the region $r<d$ and of the same form as $a \geqslant A_L$ in (A 4) in the region $r \geqslant d\sqrt{2}$. Between these two concentric circles, i.e. $d \leqslant r < d\sqrt{2}$, $f=0$ inside the $2d \times 2d$ square. Accordingly, in this region (A 4) must be weighted by the ratio of the area that is outside the invalid square (shaded area in figure 19) and the total area. Consider a circle of radius r, such that $d \leqslant r < d\sqrt{2}$. The total perimeter of the circle is $2\pi r$, of which $8(r \arccos(d/r))$ remains outside of the square. The ratio, $4\arccos(d/r)/\pi$, correctly becomes zero at $r=d$ and 1 at $r=d\sqrt{2}$. The p.d.f. is

$$f(a;\lambda)=\frac{1}{\beta}\begin{cases}\lambda \mathrm{e}^{-\lambda a}, & a \geqslant \pi(d\sqrt{2})^2\\ \lambda \mathrm{e}^{-\lambda a}\dfrac{4}{\pi}\arccos\left(d\sqrt{\dfrac{\pi}{a}}\right), & \pi d^2 \leqslant a < \pi(d\sqrt{2})^2\\ 0, & a<\pi d^2\end{cases}, \tag{A 11}$$

where

$$\beta=\int_{\pi(d\sqrt{2})^2}^{\infty}\lambda \mathrm{e}^{-\lambda a}\,\mathrm{d}a+\int_{\pi d^2}^{\pi(d\sqrt{2})^2}\lambda \mathrm{e}^{-\lambda a}\frac{4}{\pi}\arccos\left(d\sqrt{\frac{\pi}{a}}\right)\mathrm{d}a. \tag{A 12}$$

Because the second integral in (A 12) cannot be solved analytically, an approximate method is required. One possible approach is to define an equivalent circle of radius r_e with the same contribution to $\langle s_{nc}\rangle_A$ (figure 19); r_e must satisfy:

$$\int_0^{r_e} r f(a)\,\mathrm{d}a=\int_{y=-d}^{d}\int_{x=-d}^{d}\sqrt{x^2+y^2}\,f(a)\,\mathrm{d}x\,\mathrm{d}y. \tag{A 13}$$

To simplify the computation, we approximate $f(a)=1$, which reduces (A 13) to

$$\frac{r_e}{d}=\left\{\frac{2}{\pi}[\sqrt{2}+\ln(1+\sqrt{2})]\right\}^{1/3}. \tag{A 14}$$

Note that $1<r_e/d<\sqrt{2}$, as expected. Now, the invalid area has been transformed from a $2d \times 2d$ square to a circle of radius r_e concentric to a hole centre. The corresponding p.d.f. is the same as (A 4), but with

$$A_L=\pi r_e^2=\pi d^2\left\{\frac{2}{\pi}[\sqrt{2}+\ln(1+\sqrt{2})]\right\}^{2/3}. \tag{A 15}$$

Substituting λ and (A 15) into (A 6) and (A 7) yields

$$\frac{\langle s_{nc}\rangle_A}{d}\approx\left\{\frac{2}{\pi}[\sqrt{2}+\ln(1+\sqrt{2})]\right\}^{1/3} + \frac{1-\operatorname{erf}\left(\sqrt{\dfrac{4\phi}{1-(8/\pi)\phi}\left\{\dfrac{2}{\pi}[\sqrt{2}+\ln(1+\sqrt{2})]\right\}^{2/3}}\right)}{2\mathrm{e}^{-4\phi/[1-(8/\pi)\phi]\left\{(2/\pi)[\sqrt{2}+\ln(1+\sqrt{2})]\right\}^{2/3}}}\sqrt{\pi}\sqrt{\frac{1-(8/\pi)\phi}{4\phi}} \tag{A 16}$$

and

$$\frac{\langle s_{nc}^2\rangle_A}{d^2}\approx\frac{1-(8/\pi)\phi}{4\phi}+\left\{\frac{2}{\pi}[\sqrt{2}+\ln(1+\sqrt{2})]\right\}^{2/3}. \tag{A 17}$$

Previously, the means of all s_{nc}/d and s_{nc}^2/d^2 were determined. Repeating the calculation with $A_L=\pi r^{*2}$, where $r^* \geqslant r_e$ is an arbitrary distance, yields the conditional

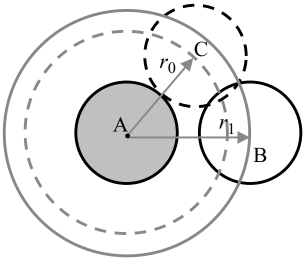

FIGURE 20. Sketch of two random coordinates (B, C) generated near random coordinate A where a hole is already assigned (solid circle).

mean of $s_{nc} > r^*$ in the random array. Applying λ and the redefined A_L to (A 6) and (A 7) yields

$$\frac{\langle s_{nc}\rangle_{s_{nc}>r^*}}{d} = \frac{r^*}{d} + \frac{\sqrt{\pi}}{4}\frac{1-\mathrm{erf}\{2r^*/d\sqrt{\phi/[1-(8/\pi)\phi]}\}}{\sqrt{\phi/[1-(8/\pi)\phi]}\,\mathrm{e}^{-(r^*/d)^2 4\phi/[1-(8/\pi)\phi]}} \tag{A 18}$$

and

$$\frac{\langle s_{nc}^2\rangle_{s_{nc}>r^*}}{d^2} = \left(\frac{r^*}{d}\right)^2 + \frac{1-(8/\pi)\phi}{4\phi}. \tag{A 19}$$

The hole surface-to-surface spacing is related to the centre-to-centre spacing as $s_n = s_{nc} - d$. Then, by definition,

$$\frac{\langle s_{nc}^2\rangle_A}{d^2} = \frac{\langle s_n^2\rangle_A}{d^2} + 2\frac{\langle s_{nc}\rangle_A}{d} - 1, \tag{A 20}$$

and $\langle s_n^2\rangle_{s_{nc}>r^*}/d^2$ can be determined by applying (A 18) and (A 19) to (A 20). The probability that a cylinder in the random array has its nearest neighbour farther than $r = r^*$ is

$$P_{s_{nc}>r^*} \equiv P(\pi r^{*2} < a < \infty) = \int_{\pi r^{*2}}^{\infty} f(a;\lambda)\mathrm{d}a = \frac{\mathrm{e}^{-\lambda\pi r^{*2}}}{\mathrm{e}^{-\lambda A_L}}, \tag{A 21}$$

where $f(a;\lambda)$ is defined by (A 4). A_L is given by (A 15). Similarly, the probability that a cylinder has its nearest neighbour within $r = 5d$ is

$$P_{s_{nc}<5d} \equiv P(0 < a < \pi(5d)^2) = 1 - \frac{\mathrm{e}^{-25\lambda\pi d^2}}{\mathrm{e}^{-\lambda A_L}}. \tag{A 22}$$

A.2. *Significance of hole generation order*

Finally, note that the above formulation underpredicts the observed A_n at large ϕ, because it does not account for the overlapping of holes other than the reference hole (hole A in figure 20). Consider the situation illustrated in figure 20, where the random coordinates are generated in the order A, B and C. Coordinate A is, by assumption, assigned as a hole centre. The coordinate closest to A is coordinate C, which is at distance r_0 from A. It is the distribution of this distance that the theory (A 4) describes. However, coordinate B, which is at radial distance r_1 from the test hole centre, is generated first. Because coordinates B and C are within d of each other, coordinate C would be discarded and the closest assigned hole centre to A would be B, at distance r_1 ($\geqslant r_0$).

Appendix B. Permeability of random cylinder arrays

The permeability, $k_\perp$, of sparse arrays can be described by Spielman & Goren (1968)'s analytical solution:

$$\frac{d^2}{k_\perp} = 8\phi \left[\frac{1}{4}\frac{d^2}{k_\perp} + \frac{d}{k_\perp^{1/2}} \frac{K_1\{(d/2)k_\perp^{-1/2}\}}{K_0\{(d/2)k_\perp^{-1/2}\}} \right], \qquad \text{(B 1)}$$

where K_j is the modified Bessel function of order j of the second kind. Koch & Ladd (1997) showed that Spielman & Goren (1968)'s solution accurately describes numerical simulation results at low ϕ, but rapidly deviates as ϕ increases beyond $\phi \approx 0.25$. Interestingly, $k_\perp \approx \langle s_n \rangle_A^2$, where $k_\perp$ is described by (B 1) and $\langle s_n \rangle_A$ is described by (A 8). The difference between the two expressions is less than 10% in the range $0.006 < \phi < 0.42$.

To the authors' knowledge, an analytical solution that describes $k_\perp$ in the range $0.3 \leqslant \phi \leqslant 0.4$ has not been developed. Least-squares fitting a function of the form $\log_{10}\{\langle \overline{f_D} \rangle / (\mu \langle \overline{u} \rangle)\} = B_0 + B_1\phi$ to numerical data in the range $\phi = 0.25$–0.44 in Koch & Ladd (1997, figure 21) yields $(R = 0.99, n = 17)$

$$\frac{\langle \overline{f_D} \rangle}{\mu \langle \overline{u} \rangle} = 10^{0.94 \pm 0.04 + (3.2 \pm 0.1)\phi}. \qquad \text{(B 2)}$$

The corresponding empirical expression for $k_\perp$ is, from (2.19),

$$\frac{d^2}{k_\perp} = \frac{4\phi}{\pi(1-\phi)} 10^{0.94 \pm 0.04 + (3.2 \pm 0.1)\phi}. \qquad \text{(B 3)}$$

Note that (B 1) and (B 3) coincide at $\phi = 0.24$ $(d/\langle s_n \rangle_A = 4.4)$. Following the above discussion, $k_\perp$ can be predicted from (B 1) for $d/\langle s_n \rangle_A \leqslant 4.4$ and from (B 3) for $d/\langle s_n \rangle_A > 4.4$.

Finally, recall from Appendix A.1 that our arrays are not exactly random. In our laboratory experiments, $k_\perp$ are predicted from (B 1) and (B 3) by matching $d/\langle s_n \rangle_A$, i.e. ϕ in the two expressions is not the actual ϕ of our array, but ϕ of an exactly random array that has the same $d/\langle s_n \rangle_A$.

REFERENCES

Baldyga, J. & Bourne, J. R. 1999 *Turbulent Mixing and Chemical Reactions*. John Wiley & Sons.

Bear, J. 1979 *Hydraulics of Groundwater*. McGraw-Hill.

Burke, R. W. & Stolzenbach, K. D. 1983 Free surface flow through salt marsh grass. *MIT Sea Grant College Program Rep.* MITSG 83-16. Massachusetts Institute of Technology, Cambridge.

Corrsin, S. 1974 Limitations of gradient transport models in random walks and in turbulence. *Adv. Geophys.* **18A**, 25–60.

Davidson, M. J., Mylne, K. R., Jones, C. D., Phillips, J. C., Perkins, R. J., Fung, J. C. H. & Hunt, J. C. R. 1995 Plume dispersion through large groups of obstacles – a field investigation. *Atmos. Environ.* **29** (22), 3245–3256.

Devore, J. L. 2000 *Probabilty and Statistics For Engineering and the Sciences*, 5th edn. Pacific Grove, California: Duxbury Thomson Learning.

Dullien, F. A. L. 1979 *Porous Media. Fluid Transport and Pore Structure*. Academic Press.

Finnigan, J. J. 1985 Turbulent transport in flexible plant canopies. In *The Forest-Atmosphere Interaction* (ed. B. A. Hutchison & B. B. Hicks), pp. 443–480. D. Reidel.

Hackert, C. L., Ellzey, J. L., Ezekoye, O. A. & Hall, M. J. 1996 Transverse dispersion at high Peclet numbers in short porous media. *Exps. Fluids* **21**, 286–290.

Han, N.-W., Bhakta, J. & Carbonell, R. G. 1985 Longitudinal and lateral dispersion in packed beds: Effect of column length and particle size distribution. *AIChE J.* **31** (2), 277–288.

Jolls, K. R. & Hanratty, T. J. 1966 Transition to turbulence for flow through a dumped bed of spheres. *Chem. Engng Sci.* **21**, 1185–1190.

Kaimal, J. C. & Finnigan, J. J. 1994 *Atmospheric Boundary Layer Flows. Their Structure and Measurement*. Oxford University Press.

Koch, D. L. & Brady, J. F. 1985 Dispersion in fixed beds. *J. Fluid Mech.* **154**, 399–427.

Koch, D. L. & Brady, J. F. 1986 The effective diffusivity of fibrous media. *AIChE J.* **32** (4), 575–591.

Koch, D. L. & Ladd, A. J. C. 1997 Moderate Reynolds number flows through periodic and random arrays of aligned cylinders. *J. Fluid Mech.* **349**, 31–66.

Lam, K., Li, J. Y., Chan, K. T. & So, R. M. C. 2003 Flow pattern and velocity field distribution of cross-flow around four cylinders in a square configuration at a low Reynolds number. *J. Fluids Struct.* **17**, 665–679.

Leonard, L. A. & Luther, M. E. 1995 Flow hydrodynamics in tidal marsh canopies. *Limnol. Oceanogr.* **40** (8), 1474–1484.

Lienhard, J. H. 1966 Synopsis of lift, drag, and vortex frequency data for rigid circular cylinders. Bulletin 300. Washington State University, College of Engineering Research Division, Technical Extension Service, Washington.

Masuoka, T. & Takatsu, Y. 1996 Turbulence model for flow through porous media. *Intl J. Heat Mass Transfer* **39** (13), 2803–2809.

Mazda, Y., Wolanski, E., King, B., Sase, A., Ohtsuka, D. & Magi, M. 1997 Drag force due to vegetation in mangrove swamps. *Mangroves and Salt Marshes* **1** (3), 193–199.

Meneghini, J. R., Saltara, F., Siqueira, C. L. R. & Ferrari Jr., J. A. 2001 Numerical simulation of flow interference between two circular cylinders in tandem and side-by-side arrangements. *J. Fluids Struct.* **15**, 327–350.

Mickley, H. S., Smith, K. A. & Korchak, E. I. 1965 Fluid flow in packed beds. *Chem. Engng Sci.* **20**, 237–246.

Nepf, H. M. 1999 Drag, turbulence, and diffusion in flow through emergent vegetation. *Water Resour. Res.* **35** (2), 479–489.

Nepf, H. M., Sullivan, J. A. & Zavistoski, R. A. 1997 A model for diffusion within emergent vegetation. *Limnol. Oceanogr.* **42** (8), 1735–1745.

Neumeier, U. & Amos, C. L. 2006 The influence of vegetation on turbulence and flow velocities in European salt-marshes. *Sedimentology* **53**, 259–277.

Nikora, V. I. 2000 Comment on "Drag, turbulence, and diffusion in flow through emergent vegetation" by H. M. Nepf. *Water Resour. Res.* **36** (7), 1985–1986.

Pearson, B. R., Krogstad, P.-Å. & van de Water, W. 2002 Measurements of the turbulent energy dissipation rate. *Phys. Fluids* **14** (3), 1288–1290.

Pereira, J. C. F., Malico, I., Hayashi, T. C. & Raposo, J. 2005 Experimental and numerical characterization of the transverse dispersion at the exit of a short ceramic foam inside a pipe. *Intl J. Heat Mass Transfer* **48**, 1–14.

Petryk, S. 1969 Drag on cylinders in open channel flow. PhD thesis, Colorado State University, Fort Collins, Colorado.

Raupach, M. R., Antonia, R. A. & Rajagopalan, S. 1991 Rough-wall turbulent boundary layers. *Appl. Mech. Rev.* **44** (1), 1–25.

Raupach, M. R. & Shaw, R. H. 1982 Averaging procedures for flow within vegetation canopies. *Boundary Layer Met.* **22**, 79–90.

Serra, T., Fernando, H. J. S. & Rodriguez, R. V. 2004 Effects of emergent vegetation on lateral diffusion in wetlands. *Water Res.* **38** (1), 139–147.

Spielman, L. & Goren, S. L. 1968 Model for predicting pressure drop and filtration efficiency in fibrous media. *Envir. Sci. Tech.* **2** (4), 279–287.

Sullivan, J. A. 1996 Effects of Marsh Grass on Diffusivity. Master's thesis, Massachusetts Institute of Technology, Cambridge, MA.

Tanino, Y. & Nepf, H. M. 2007 Experimental investigation of lateral dispersion in aquatic canopies. In *Proc. 32nd Congress of IAHR* (ed. G. Di Silvio & S. Lanzoni).

Tanino, Y. & Nepf, H. M. 2008 Laboratory investigation of mean drag in a random array of rigid, emergent cylinders. *J. Hydraul. Engng* **134** (1), 34–41.

Taylor, J. R. 1997 *An Introduction to Error Analysis. The Study of Uncertainties in Physical Mesurements*, 2nd edn. Sausalito, California: University Science Books.

Tennekes, H. & Lumley, J. L. 1972 *A First Course in Turbulence*. The MIT Press.

TUMMERS, M. J. & PASSCHIER, D. M. 2001 Spectral analysis of biased LDA data. *Meas. Sci. Technol.* **12**, 1641–1650.

VALIELA, I., TEAL, J. M. & DEUSER, W. G. 1978 The nature of growth forms in the salt marsh grass *Spartina alterniflora*. *Am. Nat.* **112** (985), 461–470.

WHITE, B. L. 2002 Transport in random cylinder arrays: A model for aquatic canopies. Master's thesis, Massachusetts Institute of Technology, Cambridge, MA.

WHITE, B. L. & NEPF, H. M. 2003 Scalar transport in random cylinder arrays at moderate Reynolds number. *J. Fluid Mech.* **487**, 43–79.

WILLIAMSON, C. H. K. 1985 Evolution of a single wake behind a pair of bluff bodies. *J. Fluid Mech.* **159**, 1–18.

YEVSEYEV, A. R., NAKORYAKOV, V. E. & ROMANOV, N. N. 1991 Experimental investigation of a turbulent filtration flow. *Intl J. Multiphase Flow* **17** (1), 103–118.

ZAVISTOSKI, R. A. 1994 Hydrodynamic effects of surface piercing plants. Master's thesis, Massachusetts Institute of Technology, Cambridge, MA.

ZHANG, H. J. & ZHOU, Y. 2001 Effect of unequal cylinder spacing on vortex streets behind three side-by-side cylinders. *Phys. Fluids* **13** (12), 3675–3686.